Characterization of low-frequency electric potential oscillations near the edge of a plasma confined by a levitated magnetic dipole.

by

Ryan M. Bergmann

Submitted to the Department of Nuclear Science and Engineering
in partial fulfillment of the requirements for the degrees of
Bachelor of Science in Nuclear Science and Engineering
and
Master of Science in Nuclear Science and Engineering
at the
MASSACHUSETTS INSTITUTE OF TECHNOLOGY
June 2009

Author .....
Department of Nuclear Science and Engineering
May 8, 2009

Certified by .....
Jay Kesner, MIT
Senior Scientist
Thesis Supervisor

Certified by .....
Darren T. Garnier, Columbia University
Research Scientist
Thesis Supervisor

Read by .....
David G. Cory
Professor of Nuclear Engineering
Thesis Reader

Accepted by .....
Jacquelyn C. Yanch
Chairman, Department Committee on Graduate Theses

Characterization of low-frequency electric potential oscillations near the edge of a plasma confined by a levitated magnetic dipole.

by

Ryan M. Bergmann

Submitted to the Department of Nuclear Science and Engineering
on May 8, 2009, in partial fulfillment of the
requirements for the degrees of
Bachelor of Science in Nuclear Science and Engineering
and
Master of Science in Nuclear Science and Engineering

Abstract

A vertically adjustable electrostatic probe array was made to observe the previously seen low-frequency angular oscillations in LDX and identify if they are related to computationally expected convective cells. The array rests one meter from the centerline and measures edge fluctuations at field lines near the separatrix. It spans ninety degrees and has 24 probes mounted on it for total probe tip separation of 6.8cm. Bispectral analysis of the fluctuations show that that an inverse cascade of energy is present at times in LDX. The cascade transfers energy from small spatial scale structures to large scale structures. The wavenumber spectrum is $\propto k^{-1.4}$ to $\propto k^{-2.5}$ at high wavenumbers, which encompasses the inverse energy cascade regime of $\propto k^{-5/3}$. The plasma also has a linear dispersion relation which gives a phase velocity of 2-16 $\frac{\text{km}}{\text{s}}$. This phase velocity is inversely correlated with neutral gas pressure in the vessel. The velocity also has a local maximum at 5 μTorr which is the pressure that produces maximum plasma density. The radial $E \times B$ drift velocities are observed to have a mean near zero, which indicates a closed structure like a convective cell. The instantaneous radial drift velocities are on the order of the ion sound speed, which is 35 km/s.

Thesis Supervisor: Jay Kesner, MIT
Title: Senior Scientist

Thesis Supervisor: Darren T. Garnier, Columbia University
Title: Research Scientist

Acknowledgments

I would like to thank Darren Garnier and Jay Kesner for the great opportunities they have given me during my stay with LDX, the lessons and experience they have shared, and the doors they have opened for me. Rick Lations and Don Strahan for their mechanical insight and assistance that saved me hours of work while constructing the probe array. Brian Grierson for his help with bispectral analysis, since it probably wouldn't be present in this thesis if he hadn't guided me. I would also like to thank my parents for their unwavering encouragement and support not only through my college and graduate years, but through my whole life. I would be nowhere without them. I would also like to thank my siblings Mike, Amy, and Becky for their encouragement, kind words, care packages, and insights. Last be not least, I would like to thank Amanda Baker for her uncanny ability to keep me sane when things looked grim and the happiness she brings into my life.

Contents

List of Figures

List of Tables

Chapter 1

Introduction

1.1 The Levitated Dipole Experiment

LDX is a concept exploration experiment being conducted at MIT's Plasma Science and Fusion Center. It aims to examine the merit of a dipole field as a potential magnetic configuration for a fusion reactor. The observation of plasmas with high kinetic to magnetic pressure ratios (β) around Jupiter spawned the idea of dipole confinement, and it has many benefits over more traditional toroids. The most notable being intrinsically high β stabilized by high compressibility and radial particle convection [3].

This thesis aims to characterize the previously observed low-frequency angular oscillations and identify if they are related to convective cells. Convection is another name for the $E \times B$ cross-field drift that occurs in plasmas. "Cross-field" means that the drift causes particles to move across magnetic field lines instead of only spiraling around a single line. The name "convection" arises from the fact that ions and electrons drift with the same speed and direction in $E \times B$ drift. Therefore, the

drift does not cause ions and electrons to separate, and the plasma is transported like a fluid in thermal convection. Electrostatic potential is constant along the magnetic field lines, so convective cells are "interchange-like" since they cause fluid elements of the plasma to swap positions in potential, or interchange.

Convective cells in plasmas are similar to conventional fluid convective cells in that they can transport both energy and mass across a gradient. In a plasma, they can cause particles to cross magnetic field lines, transporting them out of magnetic confinement [19]. The reason for studying whether convective cells occur in LDX comes from their ability to transport plasma between the core and edge of the plasma. A common problem in tokamaks is the removal of fusion products, or ash, from the hot plasma to keep the fusile particle density high enough to maintain fusion. Previous computational models similar to the magnetic configuration in LDX have yielded results where convective cells transport particles without transporting energy [22] [12]. If convective cells occur in a dipole geometry naturally, they could prove advantageous since they could remove ash from the center without decreasing the temperature of the plasma [12]. This would be a strong positive feature of dipole confinement, and would be illustrated by experimentally demonstrating that the particle confinement times are smaller than the energy confinement times.

Another property that convective cells create in a dipole geometry is that they can peak the temperature and density profile in the center, which is ideal since this localizes where fusion could occur, eases the damage done to the vessel walls, and reduces the sputter contamination from the walls.

Previous probe data from LDX indicate that low-frequency potential fluctuations occur [2], but the probes were too distantly spaced to properly capture the phenomenon with enough spatial resolution. I constructed a vertically movable probe array with tight angular spacing to provide more spatial information in hopes to

differentiate whether the potential fluctuations are convection related or related to some other phenomenon. It consists of 24 individual floating potential probes and sits on the bottom of the vacuum vessel one meter from the vessel's center with the probes extending upward. It is adjustable in the types of probes mounted on it and the vertical height they intersect the underside of the plasma. The vertical height is remotely adjustable, and can be changed during or between shots for probe insertion scans. The probe modularity allows other kinds of probes to be inserted into the array at another time.

The goal of the research is to observe the toroidal edge potential fluctuations in LDX, determine their spatial and temporal modes, report the conditions under which they arise, and characterize the energy transport between modes. The results are compared to both well-known and new computational models to determine if the fluctuations are related to convection, and to basic laws governing turbulence to see if similar turbulence is occurring in LDX. Edge measurements were taken since they describe the characteristics of energy and particle transport at the surface where the plasma interacts with the outside environment. This area is important in determining the effects that the potential fluctuations have on confinement times. The probes also would not be able to withstand the heat flux of the more dense interior plasma and would either melt to start emitting electrons, both of which would make the measurements unpredictable. The higher density of the plasma's interior is also believed to reduce the fluctuation magnitude, so edge measurements produce the best fluctuation results.

1.2 Energy Cascades

The LDX plasma is essentially two-dimensional due to it having equal potential on a field line ($\nabla\Phi \cdot \mathbf{B} = 0$). This gives rise to unusual phenomenon when inspecting turbulence in the flow equations. One phenomenon is the cascade of energy from small-scale turbulence to large-scale turbulence. Three-dimensional fluids dissipate the energy in flows into smaller-scale structures, which eventually turns macroscopic kinetic energy into thermal energy. However in two dimensions, the equations suggest that energy is taken from small-scale flows and given to large-scale ones, producing a so-called "inverse cascade" of energy. This is a counter-intuitive phenomenon in that small perturbations in the fluid are dissipative and large-scale ones grow, turning microscopic energy into macroscopic flows. Such flows are important in LDX in that they could give rise to zonal flows which increase particle confinement.

Grierson, et. al. have observed the inverse engergy cascade in Columbia University's CTX, which produces a plasma confined by a supported dipole magnet [6]. The analysis examined temporal frequencies, which were assumed to correspond to spatial modes. In addition to investigating convective cells, this thesis also sets out to determine the agreement between measuring floating potential fluctuations captured by the probe array in time and space, and examining the direction of the energy flows between spatial modes.

1.3 Electrostatic Probe Array

The electrostatic probe array is composed of twenty-four cylindrical, tungsten-tipped floating potential Langmuir probes. The array is positioned at a radius of one meter and sweeps out a ninety degree arc at the bottom of the LDX vacuum vessel. This

gives a probe separation of about 7 centimeters, giving the array a resolution of 14 centimeters. This resolution corresponds to a detectable mode number range of 1 to 46. The flow velocities arising from $E \times B$ drifts can be measured by computing the electric field from the plasma potential, and the energy cascades computed from the evolution of the spatial wavenumber spectrum.

Chapter 2

Theory

2.1 Probes

Langmuir probes are tools that measure the electrical characteristics of plasmas, and are among the oldest and simplest kinds of plasma diagnostics. In a general sense, a probe is simply an electrode placed within the plasma, as figure 2-1 shows. To get a local measurement, they are shielded from the plasma by a non-conductive material with a high melting point, typically a ceramic. Some types of probes simply measure the potential the electrode develops while in the plasma, others bias the electrode to a fix potential and measure the current drawn by it, and still others apply a time-varying potential to measure the whole I-V characteristic curve of the plasma. The probes in the LDX probe array are the floating potential variety, meaning they have a large resistor in series with the electrode. This is done to keep the current flowing in the probe low so that the electrode "floats" up to a potential called, surprisingly, the floating potential.

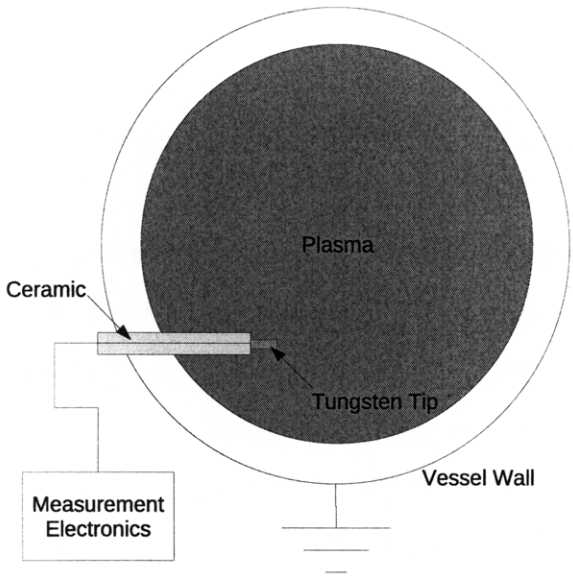

Figure 2-1: Schematic of a Langmuir probe.

2.1.1 Floating Potential

Ideally, the probes would measure plasma potential directly, but since they are not completely transparent to the plasma, they perturb the local environment they are placed in. An ideal probe draws no current, but even so it is not at the same potential as the plasma. This is due to the mass difference of the ions and electrons. Assuming their temperatures are equal, the electrons have a much higher velocity than the ions due to their smaller mass. Therefore, an electrode placed in the plasma would collect many more electrons than ions and emit a net current. Since the ideal floating probe does not allow current to pass through it, the current causes the electrode to charge up to a negative potential until sufficiently many electrons are repelled to equalize the rate at which ions and electrons are collected [10].

$$V_p = V_f + T_e \sqrt{\ln\left(\frac{M}{2\pi m}\right)} \cong V_f + 2.5T_e \text{ (for a deuterium plasma)} \qquad (2.1)$$

The floating potential is related to the plasma potential by equation 2.1, where T_e is the electron temperature, V_f is the floating potential, V_p is the plasma potential,M is the ion mass, and m is the electron mass [17]. In LDX, the electron temperature is approximately 25 eV, so the plasma potential is really about 75 volts higher than the measured floating potential. However, since its is an additive term, it does not affect the analysis of the fluctuations or the magnitude and direction of the electric field.

The potential measured directly from the probes is also not the floating potential. The probes are not ideal and draw a small amount of current. The current drops the measured potential from the actual floating potential as if there were another resistor between the probe tip and the floating potential. To get the real value of the floating potential, the slope of the linear region of the plasma's I-V curve (the plasma resistance) must be known. There are other probes in LDX that "sweep," i.e. they are driven with a certain potential waveform and the current flowing in the probe is measured. This way, the I-V curve of the plasma can be measured with a single probe while only sacrificing time resolution. As long as the plasma is relatively constant during the sweep period, the measurement is valid and can still measure time changes that take longer than a sweep period. To get an idea of the typical size of the resistance in LDX, a swept probe signal was taken from shot 81217011 and the slope of the linear portion was taken to be the resistance. The portion of the curve at higher voltages corresponds to "electron saturation," where the the electrons being drawn into the probe start repelling ions as well as creating

a current, and the net current formed departs from linearity. This shot was chosen since it was a "wedding cake" shot in that it uses all of the heating sources in different configurations. First 2.5KW of 2.45GHz ECRH was turned on, then 2.5KW more of 6.4GHz, and then 10KW more of 10.5Ghz for a total of 15KW. The resistance decreases with more heating, and has a maximum value of about 5.4 KΩ for cooler plasmas. With this resistance, $V_{\text{plasma}}/V_{\text{float}} = \frac{R_{\text{probe}}}{R_{\text{probe}}+R_{\text{plasma}}} = \frac{(1M+10k)}{(1M+10k)+5.4k} = .995$. This is a multiplicative correction, so it can affect the magnitude of the fluctuation and electric field measurements. Therefore, it is important to keep its value close to one. The resistor in the probe was chosen to be much larger than the plasma resistance, so that the multiplicative term is close to one and the floating potential can be closely approximated by the measured potential.

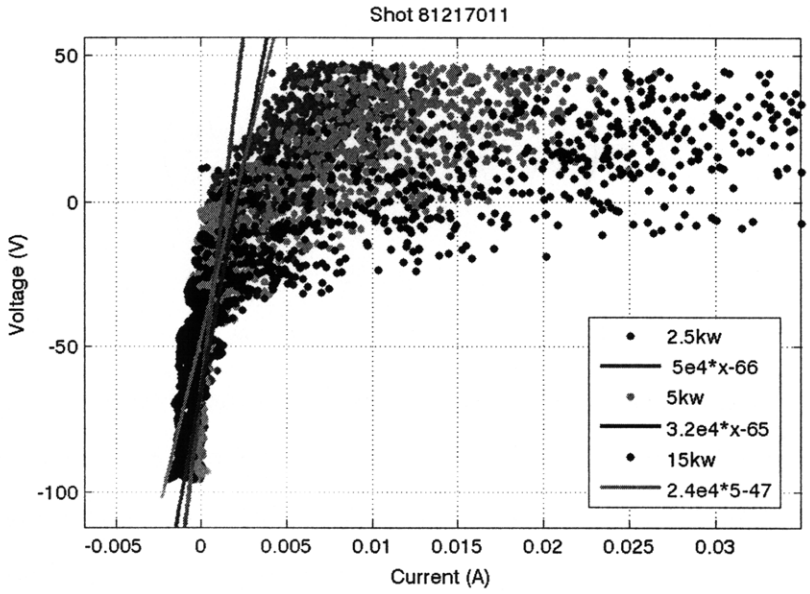

Figure 2-2: I-V curve of a typical LDX plasma, shot 81217011

2.1.2 Frequency Response

The probes need to measure potential fluctuations, so their response time must be faster than the regime of interest. Having a very large resistor in the probe is problematic if it causes the RC time of the probe to become unacceptably large. Placing the resistor close to the probe tip reduces the capacitance of the probe, but there is still a small amount of capacitance associated with the sheath and the cabling. The capacitance of the sheath is 0.13pF as by equations 2.2 and 2.3 [11] [4]. λ_D is called the Debye length, and is the characteristic length for which perturbative effects from te probe take place. The coefficients a and b in equation 2.3 depend on electron temperature, but the equation can be further approximated to only depend on the plasma sheath area A_s and the Debye length. The sheath area is the surface area of the probe if it had a radius about five Debye lengths, making the capacitance proportional to another characteristic length, A_s/λ_D.

$$\lambda_D = \left(\frac{\epsilon_0 T_e}{e^2 N_\infty}\right)^{\frac{1}{2}} = 2.35 \times 10^{-5} \left(\frac{T_k}{n_{20}}\right) \tag{2.2}$$

$$C(V_f) = \frac{a}{b}\left(\frac{A_p}{4\pi\lambda_D}\right) \approx \frac{\epsilon_0 A_s}{5\lambda_D} \tag{2.3}$$

Together with the sheath resistance of 5.4KΩ, an ideal probe would have a response time of about 0.7ns or 230MHz. The capacitance of RF coaxial cable is about 30pF per foot, which typically has a grounded shield very close to the conductor. The cables inside the array have no shields and enamel insulation and therefore should have much lower capacitances than equivalent runs of coaxial cable. The resistor is less than two feet from the probe tip, so a very conservative estimate of the cable capacitance is 1pF. Together with a series resistance of 1MΩ, this gives the probes

a -3db rolloff at $f_{-3db} = \frac{1}{2\pi RC} = 160\text{KHz}$. This lower bound of the frequency knee intrinsic to probe electronics is well above the digitization rate and the frequencies of interest, and therefore it will not affect the measured signals.

2.2 Inverse Energy Energy Cascades in Plasma Fluctuations

Analysis done by Grierson, et. al. at Columbia University's dipolar plasma in CTX inspired similar investigations in LDX. In order to measure the energy cascades in LDX, a signal from a model plasma had to be made to test the analysis method. A set of equations have been written by Hasegawa and Mima to describe the turbulence found in magnetized, nonuniform plasmas that have an electron temperature much higher than the ion temperature, where the time scales are much longer than an ion cyclotron period, and the turbulence is high enough that the wave-particle iterations are negligible [8]. Their turbulence equations were used to create a synthetic data signal similar to turbulent plasma that has nonlinear wave-wave coupling effects. This signal was used to test the analysis methods explained in the next section.

They derived these equations to explain the broad frequency spectrum observed in tokamaks that couldn't be explained by weak turbulence theories which assume a small departure from linear eigenmodes (and therefore have strongly peaked spectra). The equations are similar to mass conservation in a fluid element, and are shown in equation 2.4 where n and n_0 are the perturbed and unperturbed densities, respectively, ω_{ci} is the ion cyclotron frequency, and $\nabla_\perp$ is the gradient perpendicular to the magnetic field. Qualitatively, the equations state that the rate of change of the particle density in a fluid element plus the net movement of particles in and

out of it is equal to zero. The velocities $\mathbf{v_E}$ and $\mathbf{v_P}$ are the $\mathbf{E} \times \mathbf{B}$ and polarization drift velocities, respectively. These equations assume that the only phenomena that transport particles are related to these two drifts, and that the parallel phase velocity is much greater than the electron thermal speed, making the parallel motion unimportant. Both drifts depend on electric field (the $\mathbf{E} \times \mathbf{B}$ being static and the polarization being time-varying), and therefore are tied to the plasma potential.

$$\begin{aligned} \frac{\partial n}{\partial t} + \nabla_\perp \cdot [n_0(\mathbf{v_E} + \mathbf{v_P})] = 0 [8] \\ \mathbf{v_E} = -\nabla_\perp \phi \times \mathbf{B_0}/B_0^2 \\ \mathbf{v_P} = \frac{1}{\omega_{ci} B_0} \left[-\frac{\partial}{\partial t} \nabla_\perp \phi - (\mathbf{v_E} \cdot \nabla_\perp) \nabla_\perp \phi \right] \end{aligned} \tag{2.4}$$

Assuming the electrons follow the Boltzmann distribution, the relation $n/n_0 = e\phi/T_e$ can be written by quasi-neutrality. It can also be shown that $\nabla \cdot (n\mathbf{v_E}) = 0$ by continuity [8]. Expanding equation 2.4 in a Fourier series gives equation 2.5 [8].

$$\begin{aligned} \frac{\partial \phi_k(t)}{\partial t} + i\omega_k^* \phi_k(t) = \frac{1}{2} \sum_{k=k'+k''} \Lambda_{k',k''} \phi_{k'}(t) \phi_{k''}(t) \\ \Lambda_{k',k''} = \frac{1}{1+k^2} (k' \times k'') \cdot \hat{z} [(k'')^2 - (k')^2] \\ \omega_k^* = \frac{-k_y T_e \partial(\ln n_0)/\partial x}{eB_0(1+k^2)\omega_{ci}} \end{aligned} \tag{2.5}$$

Hasegawa and Mima also cover the consequences of this model, saying that that the mode coupling will rotate the plasma in the plane perpendicular to the magnetic field. They also mention that large potential amplitude convective cell modes were directly excited by drift-wave turbulence in their computer simulations. This suggests that convective cells not only coexist with turbulence characterized by the Hasegawa-Mima equations, but could be powered by it. Due to their similarity to

the Navier-Stokes equations, the Hasegawa-Mima equations could lead to an inverse energy cascade that concentrates energy into low wavenumbers [8], and will obey Kraichnan's power laws shown in equation 2.6 [9].

$$\begin{aligned} E(k) &= C\epsilon^{2/3}k^{-5/3} \\ E(k) &= C'\eta^{2/3}k^{-3} \end{aligned} \tag{2.6}$$

In Kraichnan, 2D turbulence is shown to conserve kinetic energy and the mean-squared vorticity (vorticity $= \Omega = \nabla^2\Sigma$, where Σ is the stream function [18]), called enstrophy. From this, the power laws in equation 2.6 were derived [15], where C and C' are dimensionless constants and ϵ and η are the rates of cascade of energy and enstrophy per unit mass, respectively. The $k^{-5/3}$ power law corresponds to a "downward" energy cascade where $\epsilon < 0$, i.e. that energy is transferred from the wavenumbers where this law holds to smaller wavenumbers with zero transference of enstrophy. The k^{-3} power law corresponds to an "upward" cascade in enstrophy, and zero transference of energy. These regimes can occur in the same spectrum, and cause energy to be transported to small wavenumbers and vorticity is transported to high wavenumbers. The downward cascade of energy implies that if high wavenumbers are excited externally, their energy will be transferred to lower wavenumbers. This gives the plasma a "self-organizing" characteristic that will cause energy from high modes excited by heating to move to large-scale structures in the plasma [15]. If the LDX plasma has these regimes, it is another indicator of fluid-like 2D turbulence and an inverse cascade of energy.

2.3 The Ritz Bispectral Method

The method derived by Ritz, et. al., is used to determine the direction, magnitude, and coupling of the energy cascades in the LDX plasma. The method assumes a stationary state, i.e. the power spectrum is unchanging. This implies that the linear growth rate of each mode is balanced by the energy transfer from nonlinear wave-wave coupling. It also is only accurate for systems where the majority of the power is in the linear and quadratic terms described by the wave coupling equation in equation 2.8. If incoherent or higher-order terms make up a large portion of the power, the computed transfer coefficients will not be accurate [21]. This equation is identical in form to equation 2.5, showing that this method is valid for characterizing the interactions that arise from the Hasegawa-Mima turbulence. The Hasegawa-Mima equations were derived for tokamaks, however, and are not directly applicable to a dipole plasma. They are useful to create a synthetic signal to test the the analysis routines using the Ritz method, as will be shown later.

$$\phi(k,t) = \sum_{k} \phi(x,t) e^{ikx} \tag{2.7}$$

$$\frac{\partial \phi(k,t)}{\partial t} = \Lambda_k^L \phi(k,t) + \frac{1}{2} \sum_{k_1,k_2} \Lambda_k^Q(k_1,k_2)\phi(k_1,t)\phi(k_2,t) \tag{2.8}$$

$$\Lambda_k^L = (\gamma_k + i\bar{\omega_k}) \tag{2.9}$$

The first step in deriving the method is Fourier transforming then replacing the differential in equation 2.8 with the finite difference shown in equation 2.11. A finite difference is basically replacing the partial derivative with the definition of a derivative. The finite difference approximation of the partial derivative is only valid

for functions of ϕ with slowly changing phase over the time interval τ [21].

$$\phi(k,t) = |\phi(k,t)|e^{i\Theta(k,t)} \tag{2.10}$$

$$\frac{\partial\phi(k,t)}{\partial t} = \lim_{\tau\to 0}\left(\frac{|\phi(k,t+\tau)| - |\phi(k,t)|}{\tau}\frac{1}{|\phi(k,t)|} + i\frac{\Theta(k,t+\tau) - \Theta(k,t)}{\tau}\right)\phi(k,t) \tag{2.11}$$

If the Fourier transform is represented in magnitude and phase in complex notation as in equation 2.10, substituting equation 2.11 into equation 2.8 yields an approximation to the wave coupling equation shown in equation 2.12.

$$\phi(k,t+\tau) = \frac{\Lambda_k^L\tau + 1 - i(|\Theta(k,t+\tau)| - |\Theta(k,t)|)}{e^{-i(\Theta(k,t+\tau)-\Theta(k,t))}}\phi(k,t) + \frac{1}{2}\sum_{k_1,k_2}\frac{\Lambda_k^Q(k_1,k_2)\tau}{e^{-i(\Theta(k,t+\tau)-\Theta(k,t))}}\phi(k_1,t)\phi(k_2,t) \tag{2.12}$$

Redefining a few quantities gives a neat expression show in equation 2.16. The quantities L_k and Q_{k_1,k_2} are the linear and quadratic transfer coefficients, respectively. They characterize the linear and quadratic processes of the system and in conjunction form the "black box" system that modifies an "input" signal X_k to produce an "output" Y_k.

$$X_k = \phi(k,t), \qquad Y_k = \phi(k,t+\tau) \tag{2.13}$$

$$L_k = \frac{\Lambda_k^L \tau + 1 - i(|\Theta(k,t+\tau)| - |\Theta(k,t)|)}{e^{-i(\Theta(k,t+\tau)-\Theta(k,t))}} \tag{2.14}$$

$$Q_k = \frac{\Lambda_k^Q(k_1,k_2)\tau}{e^{-i(\Theta(k,t+\tau)-\Theta(k,t))}} \tag{2.15}$$

$$Y_k = L_k X_k + \frac{1}{2}\sum_{k_1,k_2} Q_k Y_k X_{k_1} X_{k_2} \tag{2.16}$$

This system is not directly invertible, and more involved methods must be used to obtain the transfer coefficients from the input and output of the system. This is due to the nonlinear nature of the system desribed by Q_{k_1,k_2}. To create a solvable set of equations, moments are built from equation 2.16. The first moment is made by multiplying equation 2.16 by the complex conjugate of X_k and ensemble averaging (denoted by $\langle ... \rangle$ in the equations) over many independent realizations. These ensemble averaged quantities are call "estimators" since the estimate the true value of the autopower, crosspower, bispectrum, et cetera by averaging many different instances of the same quantity. An individual measurement may be far from the true value, but averaging over many should make the value converge to the true value. Its like computing the temperature of a material by measuring and averaging the kinetic energy of individual molecules.

$$\langle Y_k X_k^* \rangle = L_k \langle X_k X_k^* \rangle + \frac{1}{2}\sum_{k_1,k_2} Q_{k_1,k_2} \langle X_k^* X_{k_1} X_{k_2} \rangle \tag{2.17}$$

$$\langle Y_k X_{k_1'}^* X_{k_2'}^* \rangle = L_k \langle X_k X_{k_1'}^* X_{k_2'}^* \rangle + \frac{1}{2}\sum_{k_1,k_2} Q_{k_1,k_2} \langle X_{k_1'}^* X_{k_2'}^* X_{k_1} X_{k_2} \rangle \tag{2.18}$$

The second moment equation is made by multiplying by $X^*_{k'_1} X^*_{k'_2}$ and ensemble averaging. This produces the fourth order moment $\langle X^*_{k'_1} X^*_{k'_2} X_{k_1} X_{k_2} \rangle$, which is a very computationally intensive quantity to compute, so a closure approximation is made assuming all off-diagonal terms $(k'_1, k'_2) \neq (k_1, k_2)$ are zero. Approximating $\langle X^*_{k'_1} X^*_{k'_2} X_{k_1} X_{k_2} \rangle$ with the second order moment $\langle |X_{k_1} X_{k_2}|^2 \rangle$ is called the Millionschikov approximation [21]. This approximation causes the summation in 2.18 to drop out, and the quadratic transfer coefficient can be directly extracted from the equation [21].

The transfer coefficients are the only unknowns in the two coupled moment equations and thus can be solved for. The transfer coefficients are given by quantities shown in equation 2.19. They can be solved iteratively by using an initial guess for L_k where $Q_{k_1,k_2} = 0$. The equations should be self-consistent and converge onto the proper transfer coefficient values for a given set of estimators [20].

$$L_k = \frac{\langle Y_k X^*_k \rangle - \sum_{k1 \geq k2} Q_{k_1,k_2} \langle X^*_k X_{k_1} X_{k_2} \rangle}{\langle X_k X^*_k \rangle}, \; Q_{k_1,k_2} = \frac{\langle Y_k X^*_{k_1} X^*_{k_2} \rangle - L_k \langle X_k X^*_{k_1} X^*_{k_2} \rangle}{\langle |X_{k_1} X_{k_2}|^2 \rangle} \quad (2.19)$$

To determine the direction on magnitude of the power transferred between coupled waves, the coupling coefficient, $\Lambda^Q_k(k_1, k_2)$ (which is equal to the transfer coefficient multiplied by the phase shift, which can be approximated by equation 2.23 [21]), is multiplied by the bispectrum and the real part is taken (shown by the "$\Re$" operator). This new quantity is called the quadratic power transfer coefficient, and is shown in equation 2.21. When it is plotted, the negative regions show the wavenumbers that have power being drawn out of them into waves with smaller wavenumbers. Positive regions show the converse, or wavenumbers that have two smaller wavenum-

bers putting power into them. Figure 2-4 shows an illustration of this three-wave breakdown/buildup process. By summing along all contributions to a single k, a quadratic power transfer function similar to the linear growth rate (eqn. 2.20 [13]) can be computing from T_k^Q, as shown by equation 2.22. These plots are shown in the results section, and represent the net power transferred into a wavenumber, k, from positive and negative contributions (buildup and breakdown) of other wavenumber pairs, k_1 and k_2's [21].

$$\gamma_k^L = \frac{|L_k|^2 - 1}{\tau} \tag{2.20}$$

$$T_k^Q(k_1, k_2) = \Re(\Lambda_k^Q(k_1, k_2)\langle\phi_k^*\phi_{k_1}\phi_{k_2}\rangle) \tag{2.21}$$

$$\gamma_k^Q = \sum_{k_1,k_2} T_k^Q(k_1, k_2) \tag{2.22}$$

$$e^{-i(\Theta(k,t+\tau)-\Theta(k,t))} \cong \frac{\langle Y_k X_k^*\rangle}{\langle|Y_k X_k^*|\rangle} \tag{2.23}$$

Ritz deals with the spatial spectra, but the method can be applied in both time and space. If temporal frequencies are examined, the signals need to come from two probes separated in space. In a mathematical sense, the spatial method compares many $\phi(k,t)$ and $\phi(k,t+\tau)$'s, whereas the temporal method compares many $\phi(x,\omega)$ and $\phi(x+\Delta x,\omega)$'s. If spatial frequencies are examined, the signals need to come from a probe array signals separated in time. The majority of the analysis done here deals with the spatial application of the Ritz method since the probe array allows direct measurement in wavenumber space. The plasma is assumed to rotate, however, and there should be a relation between the wavenumbers and frequencies shown in either analysis. I will discuss the time method first since the routines were tested with "time-like" synthetic signals. It is easier to create synthetic time sig-

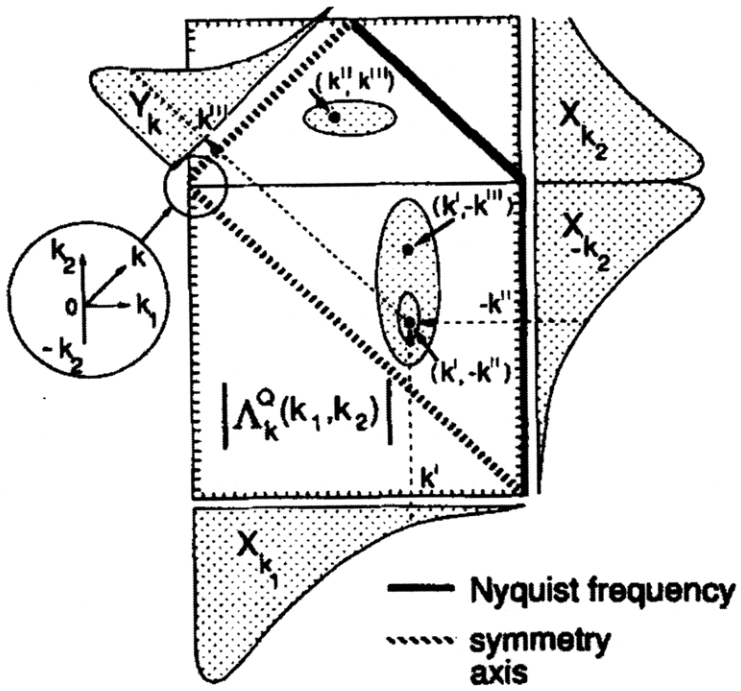

Figure 2-3: Graphical description of how the quadratic coupling coefficients relate to the input and output signals taken directly from Ritz. The figure shows how a set of wavenumbers that satisfy the condition $k = k_1 + k_2$ are multiplied by the value of $Q_k(k_1, k_2)$ and summed to produce the resultant value of k. It highlights the areas of the coupling coefficient like lines of constant k, Nyquist cutoffs, and symmetry axes. [21]

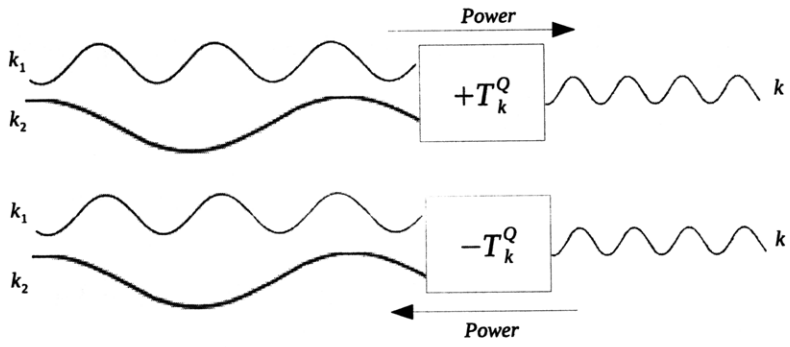

Figure 2-4: Illustration showing how the three waves interact depending on the sign of T_k^Q

nals and this is the only reason it was tested in time rather than in space. If the algorithms are valid for time analysis, they should also work for space since the only difference between the two is along which dimension the Fourier transform is made.

The method in time space starts by taking the fast Fourier transform (FFT) of the two input signals and normalizing (dividing) the transform by its length. These two signals are offset by a distance Δx in space. The signal is assumed to have gone through a linear and non-linear change described by a "black box" operation during the distance Δx, shown in figure 2-9. The input to the black box is the signal measured at x and the output is the the signal measured at $x + \Delta x$. From these two long time signals, small samples are taken at equal times and used to compute the estimators. The window is then moved down the signal and the estimators are recomputed. Figure 2-5 shows this process diagrammatically. The set of estimators acquired by this process make up the ensembles used to compute the ensemble averaged estimators and ultimately the transfer coefficients.

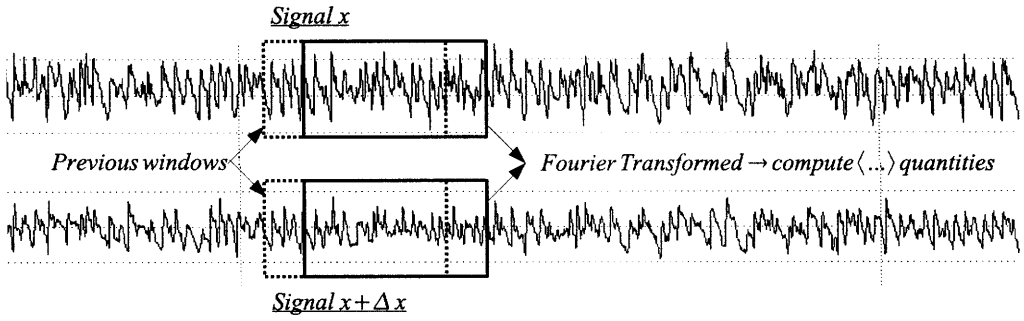

Figure 2-5: How samples are taken from two time signals to make ensembles.

To test the method, a synthetic signals had to be made where the linear and quadratic transfer coefficients were know a priori. Such a signal set was created by using Fourier transformed Gaussian random noise to excite the "black box" system described by equation 2.16 then inverse Fourier transforming the input and output

signals back into time. A large number of points had to be used in constructing the signal so sampling the signal in time with a moving window would produce a reasonable approximation. The ideal signal is continuous, so the appropriate length the synthetic signal needed to be was determined by sampling theory.

Sampling can be thought of as multiplying a function with a Dirac comb function. Since multiplication in normal space is convolution in Fourier space, sampling a signal with a finite Dirac comb is the same as convolving its frequency spectrum with the transform of a finite comb. The Dirac comb is simply a train of Dirac delta functions, and its Fourier transform is a complex exponential. Since the Fourier transform is a linear operator, the Fourier transform of a finite comb is simply a sum of harmonic complex exponentials with the fundamental at the sampling width, T, and the last harmonic at half the sample points, $\frac{N}{2}$, as shown in equation 2.24. The sum of complex exponentials converges to a dirac comb function with spacing $\frac{1}{2\pi T}$, shown in figure 2-6. For the signal to be perfectly reconstructed in frequency space, the width of the frequency space comb must be twice as wide than the highest frequency present in the signal (the Nyquist sampling theorem).

$$\text{comb} = \sum_n \delta(x - nT) \qquad \mathfrak{F} \Rightarrow \qquad \text{COMB} = \sum_n e^{iknT} \tag{2.24}$$

If this condition is satisfied, then the convolution will produce a train of spectra that do not overlap, i.e. every frequency is perfectly resolved. The effect of truncating the comb in normal space is that the sum of sine waves in frequency space is also truncated, and therefore the sampling kernel is not a perfect Dirac delta. The resulting pseudo-delta has some finite width from truncation, and smears out the details of the frequency spectrum when the signal is convolved in frequency space. Figures 2-7 shows the sampling kernels corresponding to sampling in normal space

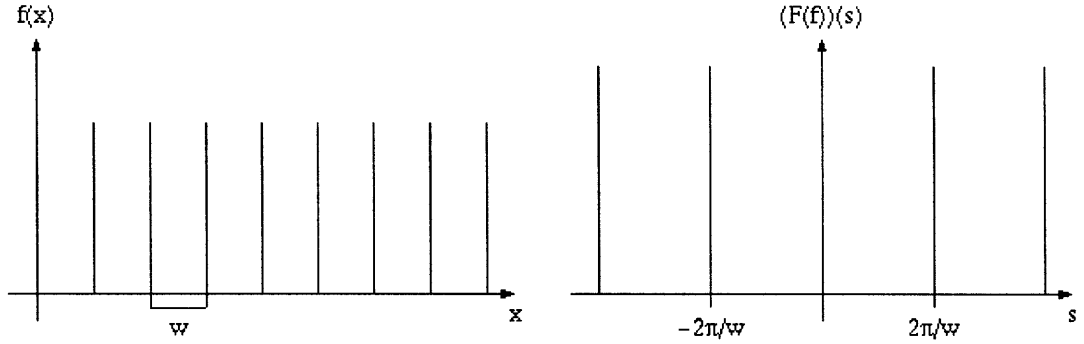

Figure 2-6: The Dirac comb function and its Fourier transform [16]

with a truncated Dirac comb. Since adding points in normal space is the same as adding additional terms to the sum in frequency space, adding two additional points in normal space is the same as adding one harmonic term in frequency space, so the first harmonic corresponds to 3 points, the second to 5 points, etc. Figure 2-8 illustrates the effect of sampling on a slightly noisy signal. The lower harmonics average over the signal by their FWHM. Using smaller windows effectively smudges out the details in the spectrum, and therefore shorter time series can be used to construct the synthetic signal if small windows are used to sample it. If wide windows are used, the imperfections in the construction will become apparent and will no longer look like the coefficients used to construct the signal. A fit to the FWHM trends of the sampling kernels yields FWHM $= 2.126/x^{.7493}$ where x is the harmonic number (or $x = \frac{samples-1}{2}$).

The experimental data has a width of 22 points (since the first and last channels were broken on installation), but is padded up to 92 points, so the analysis was tested with a window of 92 points. Using a very conservative 100 signal widths within one window width, a synthetic signal width of $s_{signal} = \sqrt[.7493]{100}(s_{sample}-1)+1 \approx 45,000$ was determined. This fact was important for computing the test case since running

the signals through the quadratic sum in equation 2.16 takes many hours to run. This in mind, the test case was done using the temporal method since only two long signals needed to be created. To directly test the spatial method, many consecutive signals needed to be made, and doing so for signals of this length would have taken months of computing time. Using the temporal method to test the code apposed to the spatial method should still give an indication if the code is working as it should.

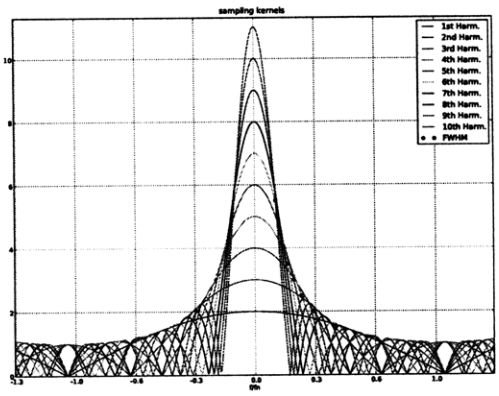

Figure 2-7: Progression of sampling kernels as more points are added in time.

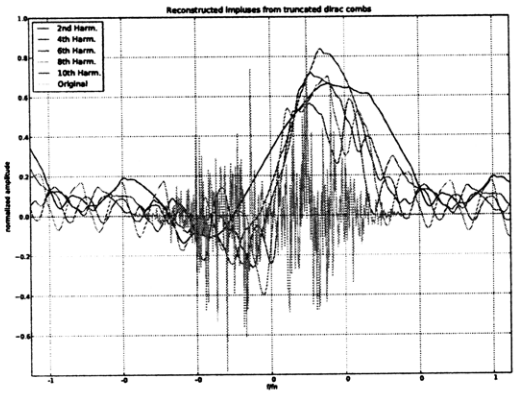

Figure 2-8: Effect of finite sampling in time on frequency spectrum construction.

The test signal was made by feeding 150,001 Gaussian random points (to absolutely ensure accuracy) through 5 black box nonlinear systems in series, and the input and output of the fifth box was used to test the analysis routines. The transfer coefficients used are shown in equation 2.25 and resemble the the form of the coefficients in the Hasegawa-Mima equations in equation 2.5 [20]. Ensembles were built by moving a window of 92 points across the time signal with an overlap of one-sixteenth of the window width. The overlap introduced phase changes large enough to enhance convergence of the ensembles. This method is useful for determining the coupling between the frequencies in LDX assuming the turbulence is well-characterized by the

Hasegawa-Mima equations and there are very few iterations other than linear and quadratic. Figure 2-9 illustrates the evolution of the random signal into the signals used to test the analysis. The input coefficients used to calculate the test signal are shown in figures 2-10 and 2-11. The curvatures of the linear and quadratic coefficients are in opposition so the system tends to an equilibrium spectrum where the two growth rates sum to zero.

$$\begin{aligned} L_k(k) &= 1 - 0.4\frac{k^2}{k^2_{\text{Nyquist}}} + i0.8\frac{k}{k_{\text{Nyquist}}} \\ Q_k(k_1, k_2) &= \frac{i}{5k^4_{\text{Nyquist}}}\frac{k_1 k_2(k_2^2 - k_1^2)}{1 + k^2/k^2_{\text{Nyquist}}} \end{aligned} \tag{2.25}$$

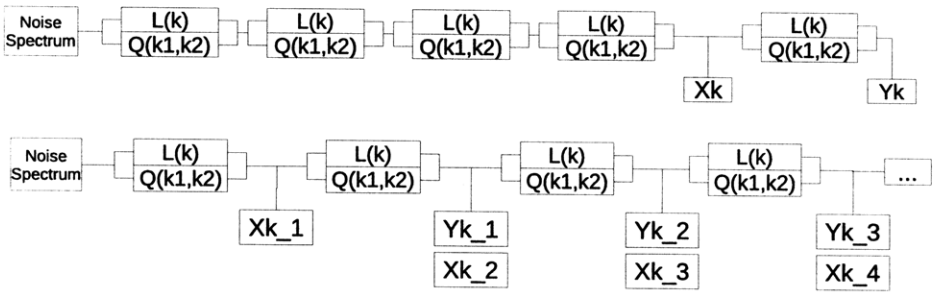

Figure 2-9: Block diagram analogous to taking temporal measurements showing the modification of an input signal by five series block box systems (top), and a diagram analogous to taking spatial measurements showing the modification of an input signal another series block box systems (bottom).

In the analysis, negative wavenumbers do not imply wave propagation in an opposite direction, they simply give an alternate amplitude and phase that can describe an identical wave as the positive wavenumber value. Therefore, including the negative wavenumber space allows all possible combinations of three wave iterations to be considered.

Since Q_k is symmetric (since the order of wavenumber addition does not matter),

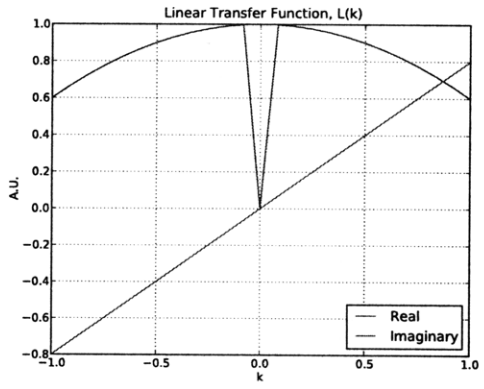

Figure 2-10: Linear transfer function used to produce the synthetic data

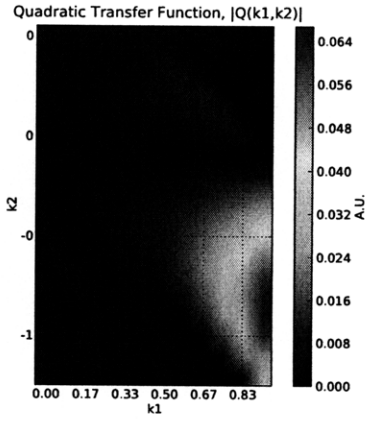

Figure 2-11: Quadratic transfer function used to produce the synthetic data

i.e. $Q_k(k_1, k_2) = Q_k(k_2, k_1)$, only the non-redundant quadrants where $k_1 \geq k_2$ are plotted in the following figures. The axis of symmetry is shown by the green dashed line and the Nyquist limit by the red dashed line. The "upper triangle" is limited by the Nyquist condition in k and the "lower triangle" is limited by the Nyquist condition in k_1 and k_2.

The plots show that the analysis routines can indeed measure the quadratic and linear transfer coefficients since the simulated and analytic coefficients have good agreement. However, the analysis carried out in most of this thesis will be the spatial kind since the probe array was constructed to directly measure spatial fluctuations. These measurements can be compared to similar temporal ones to ensure agreement or to point out interesting differences.

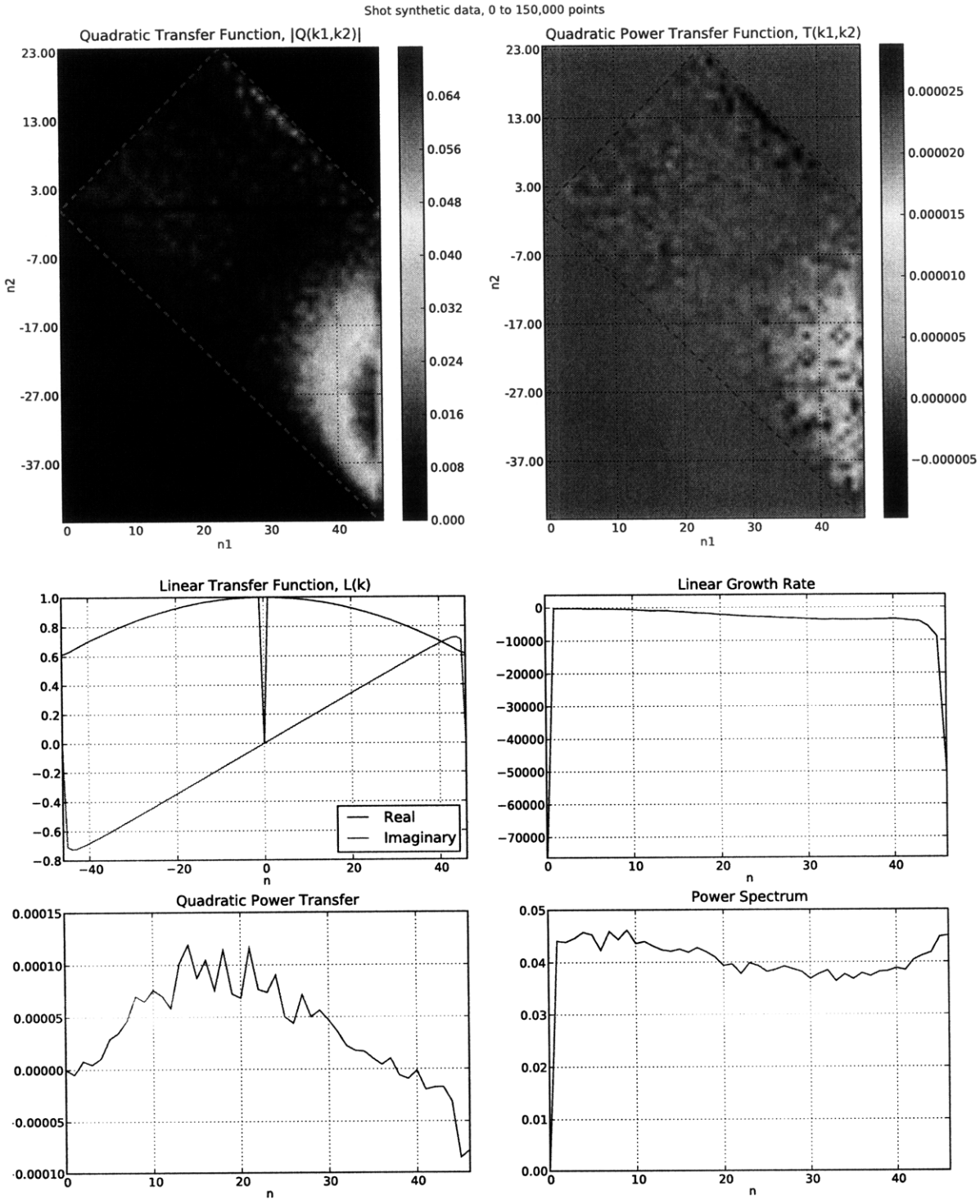

Figure 2-12: Quadratic and linear transfer functions, linear growth rate, quadratic power transfer, and power spectrum computed from the synthetic test data.

2.4 Phase Velocity, Drifts, and Wavenumber Spectrum

The data collected by the probe array can be used for more direct analysis than the Ritz bispectral method. The plasma rotation speed can be calculated directly from stripey plots, which simply plot the probe fluctuation amplitude versus time. The phase speed is simply the slope of the line when the probe number is scaled to distance. If the plot is extended to 2π, or 92 probes, the mode number in the plasma can also be determined by the number of times a line on the stripy plot overlaps itself. Since the array spans $\frac{\pi}{2}$ radians, the resolution spectrum created by taking the FFT of the 22 data points is only 4 mode numbers, despite having a Nyquist frequency at n=46. Most of the phenomena of interest is at low-frequencies, so the resolution of the signal is increased by padding the input signal from the array to 92 points (which corresponds to 2π radians) with zeroes. This way, the FTT has a resolution of 1 mode number and each mode can be distinguished. Padding is in essence the same as interpolating the stripey plot to determine the mode numbers.

$$\vec{E} = -\nabla\Phi \tag{2.26}$$

$$\vec{v}_{E\times B} = \frac{\vec{E}\times\vec{B}}{B^2} \tag{2.27}$$

$$\vec{v}_{\text{plasma}} = R\frac{\partial\theta}{\partial t} \tag{2.28}$$

The wavenumber power spectrum itself if also of interest, and can be measured by averaging the autopower spectrum, $\langle X_k X_k^* \rangle$, over a time interval. From this, it can be measured if the spectrum obeys the power laws stated in Kraichnan, and if

it is suggestive of inverse energy cascades. The dominant modes are also easily seen from the power spectrum, and determining their common values and relation to the frequencies present is important information.

Since the potential is measured by the probes, the azimuthal/toroidal electrical field can be directly determined from the gradient of the potential as shown in equation 2.26 [7]. The elctric field can be used to compute the $E \times B$ drift velocity, as shown in equation 2.27 [4] . These drifts are directly related to convection, and measuring their magnitude shows its strength in transporting particles to and from the core of the plasma.

Chapter 3

Experimental Setup

The LDX vacuum vessel is a large, puck-shaped, half inch thick stainless steel chamber. It has is three meters tall, 5 meters in diameter, and has a volume of about 65 cubic meters. High vacuum is established in the chamber by means of turbo- and cryo-pump systems. Figure 3-1 Shows a cutaway of the vacuum vessel and highlights the main components of LDX.

The magnetic dipole field is created by the floating coil, or "F-coil," which is levitated in the center of the vacuum chamber during plasma shots. Levitation clears the path inside the coil ring, and allows particles to move freely along the entire field line. This reduces particle losses and improves confinement times. The F-coil must be able to stay levitated for an extended period of time and cannot have any external connections to keep current flowing in it. Therefore it is made of the low temperature superconducting material Nb_3Sn and be charged inductively. The F-Coil weighs 565 kg, is cooled with helium, and can remain superconducting for up to 2.5 hours [1].

During a run, the F-coil is charged by a second coil located underneath the

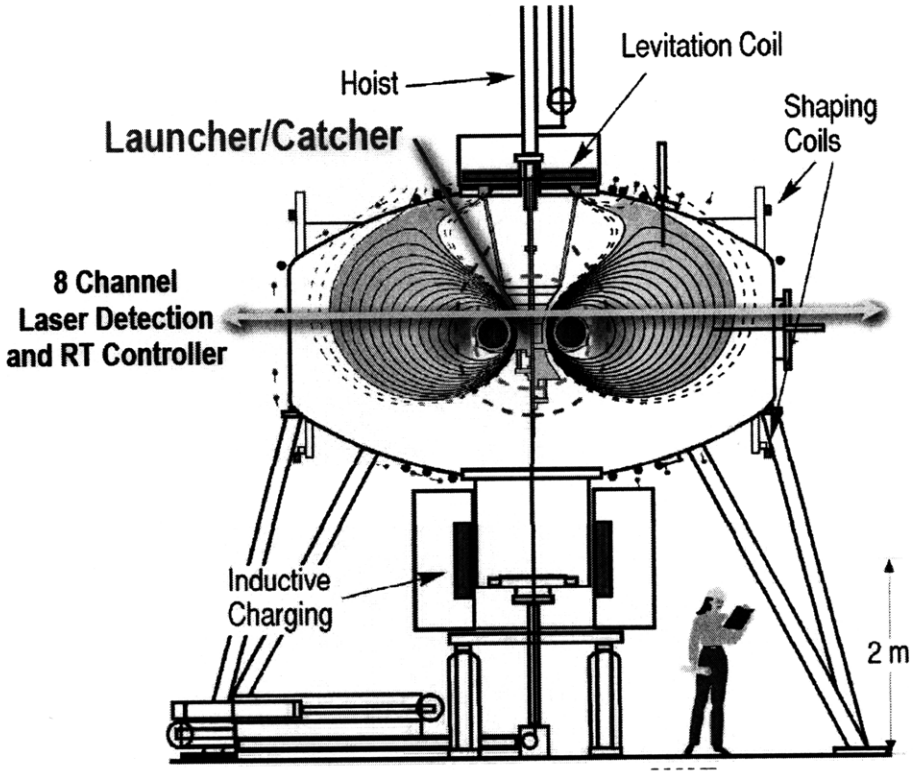

Figure 3-1: A cutaway of the Levitated Dipole Experiment. This view shows the floating coil in the center of the vacuum vessel, levitation coil on top of the vessel, charging coil inside the charging station underneath the vessel, launcher/catcher, and laser position system.

vacuum vessel. This coil is called the charging coil (C-coil), and is made of another low-temperature superconductor, NbTi. The warm, non-superconducting F-coil rests inside the C-coil prior to charging while the C-coil is charged to 425 amperes (3.6 MA-turns). Then the F-coil is cooled with helium, which makes it superconducting, and the C-coil is discharged. This causes current to flow in the F-coil. The F-coil is then raised to the middle of the vacuum vessel mechanically. A third, copper coil on top of the vessel is turned on to levitate the F-coil, and its mechanical supports are backed away. At this point, LDX is ready to make plasmas [1].

Plasmas are made by releasing a small amount of gas (deuterium or helium) into the vessel before high power microwaves are injected. The microwaves ionize the gas by means of ECRH (electron cyclotron resonance heating), where most of the power is absorbed by electrons that have a cyclotron frequency the same as the microwave frequency. The microwaves therefore heat the plasma at shells of constant field strength. The microwave powers and frequencies using in LDX are 2.5 kilowatts of 2.45GHz, 2.5 kilowatts of 6.4GHz, and 10 kilowatts of 10.5GHz. The microwaves themselves are weakly attenuated by the plasma, so they bounce inside the vessel many times before being dissipated. By this reflection mechanism, the microwaves heat the plasma isotropically [1].

The probe array enters the vessel through a port on the bottom southwest side of the vessel. The tips of the probes are at a constant 1 meter radius, and can be positioned from -65cm to -45 cm from the midplane. Figures 3-2-3-4 show the position of the array with respect to the floating coil and the magnetic fields. The probe is usually positioned close the the "seperatrix" during plasma shots. "Seperatrix" is another word for the last closed field line. Inside the seperatrix, particles can stream along a field line without being lost. Outside the seperatrix, field lines intersect objects, and a particle streaming along a field line is almost immediately lost. Figures

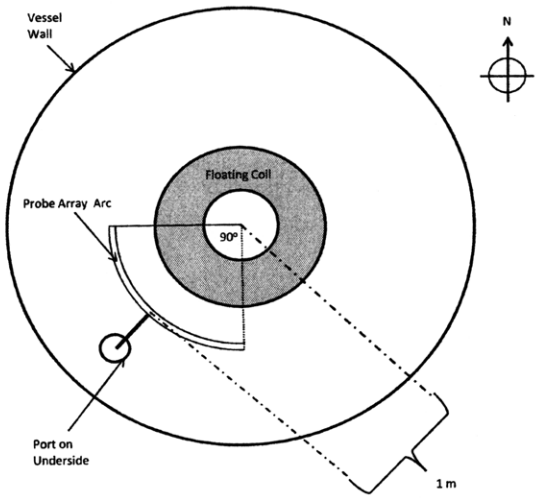

Figure 3-2: Top-down view of LDX's midplane showing the position and extent of the probe array arc.

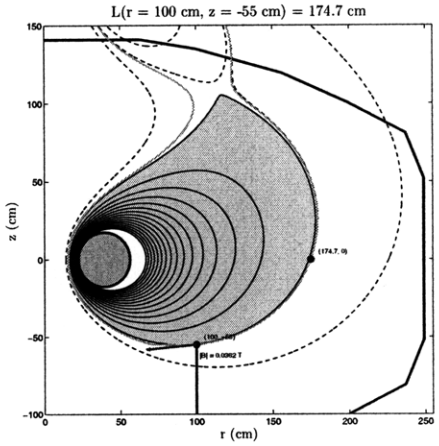

Figure 3-3: The probe array position relative to the field lines at the separatrix. The red line shows the direction of the magnetic field at that point. The ExB direction measured by the array is at a right angle to the red line, pointing radially inwards. The blue line shows the field line intersecting the probe tip.

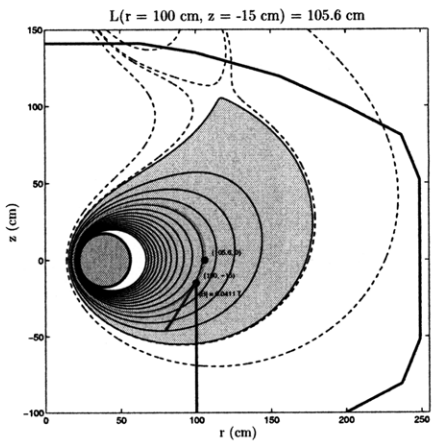

Figure 3-4: The probe array position relative to the field lines at full insertion. The red line shows the direction of the magnetic field at that point. The ExB direction measured by the array is at a right angle to the red line, pointing radially inwards. The blue line shows the field line intersecting the probe tip.

3-3 and 3-4 show the region inside the seperatrix in pink.

3.1 Probe Array Design

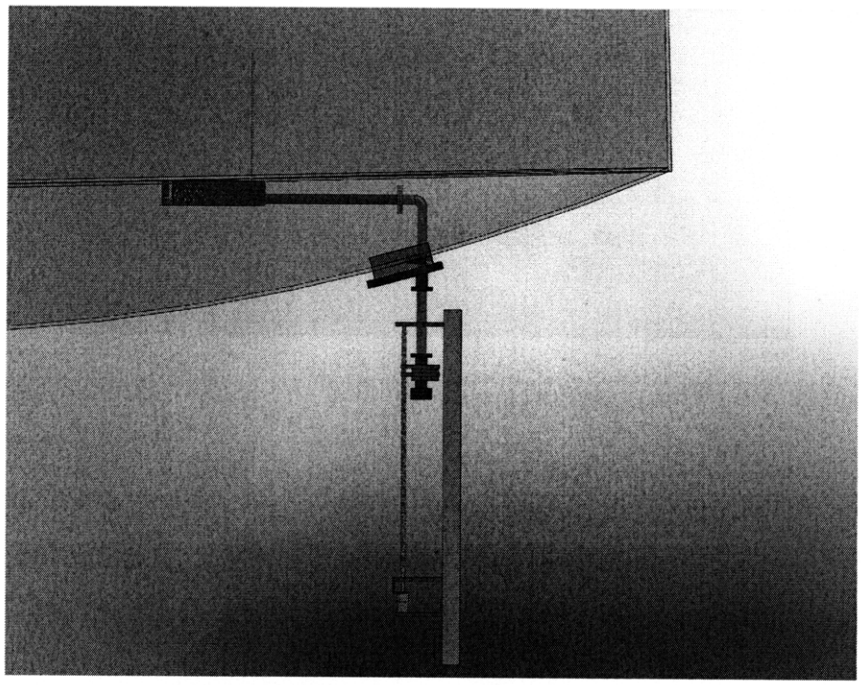

Figure 3-5: SolidWorks model of the entire array system.

3.1.1 Mechanical

Construction

The floating potential probes alumina ceramic tubes with long tungsten tips. The ceramic has 16 inches of exposed length from the top of the array arc. This length was chosen so the tips are 10 cm out of the separatrix when fully extracted (the array hits the bottom of the vessel).

The positioning of the probe array is critically important since the plasma fluctuations under investigation occurs near the edge. The probe tips are one centimeter of exposed 0.125 inch diameter, 2% thoriated tungsten, which required them to be

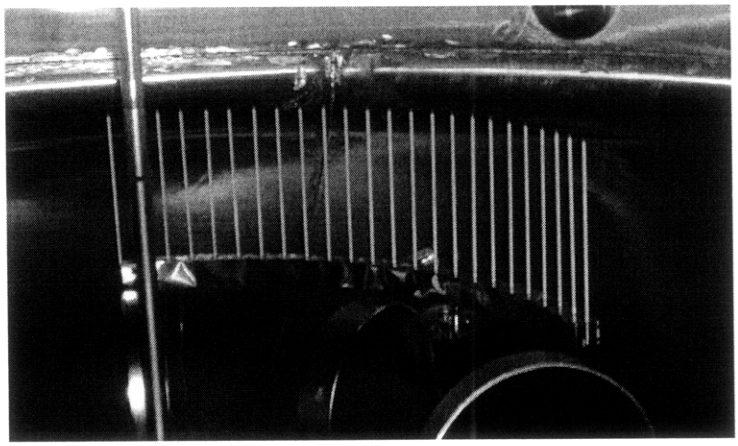

Figure 3-6: The probe array installed in the LDX vacuum vessel.

placed at a position with half centimeter accuracy. The structure of the array arc was designed to keep the probe tips positioned accurately by reducing lever arm errors due to the flexing of the support materials under gravity.

SolidWorks was used to simulate the probe array structure under gravity. A box-like structure was initially attempted to create a rigid arc without much weight. This designed was improved upon by making the back wall 0.3185 inches thick, the top and bottom walls 0.109 inches thick, and cutting out a pattern of holes in the back wall. The circular holes have a hexagonal distribution and an area that increases exponentially approaching the ends of the arc. Less weight is supported further out , so less material is needed to support it. Using this pattern greatly reduced the total weight of the structure without sacrificing much strength, and therefore reduced the amount of flexion it experiences under gravity.

Since there needs to be access to the wiring in order to swap probes, the front edge of the array arc is supported by 0.25 inch diameter tubes instead of a large plate. This allows easy access to the array internals while keeping the structure rigid and reducing total weight. A 20 mil plate of 316 stainless steel was placed over the

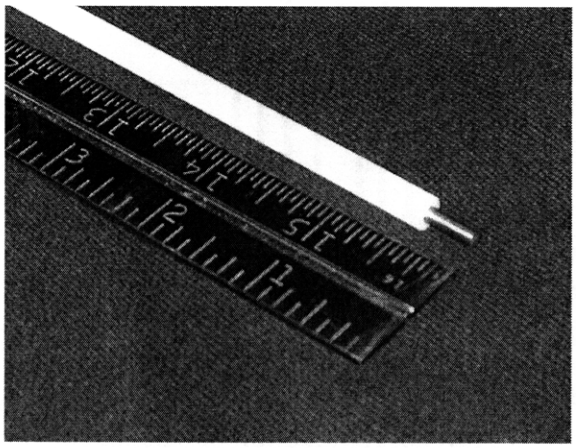

Figure 3-7: A probe tip.

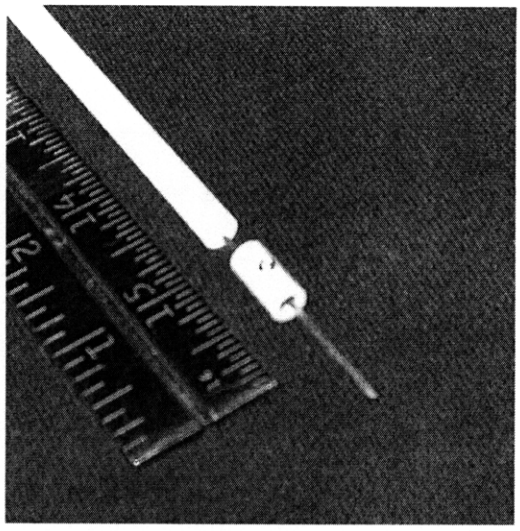

Figure 3-8: The PEEK insulator and solid copper conductor.

front to protect the wiring from the plasma. This plate is tack welded so it could be easily removed if access is needed.

The probes are held into the array arc by stainless steel holders like that shown in figure 3-10. The holders are welded to the bottom of the arc's top plate and use set screws to secure the probes' ceramic housing to the arc. There is a set screw in the PEEK insulator at the bottom of the holder which fixes the length of tungsten electrode protruding from the probe tip while keeping the conductor electrically isolated. The copper conductor is passed out through the holder's bottom and is terminated in a pushpin connector. A 1 megaohm resistor is connected in series with the conductor with similar pushpins and sockets for easy removal. The resistor is connected to a socket clamped into a ceramic terminal block which is hardwired to the a 32-pin vacuum feedthrough.

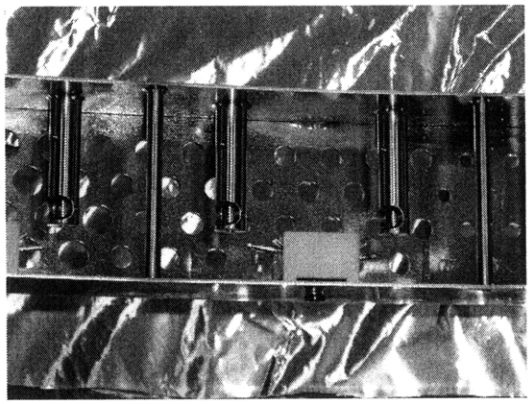

Figure 3-9: Closeup of the probe array without the front shield. This view clearly shows the cutout pattern of the back rib, the probe holders, the front braces, and the ceramic terminal blocks

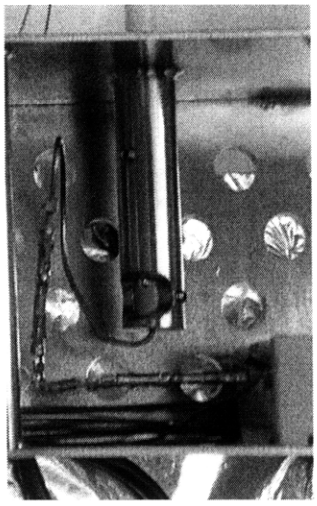

Figure 3-10: Detail of the probe holder and terminal block highlighting the resistor and connection pins/sockets.

Movement

The probe array's drive system is composed of a ball screw attached to a vacuum nipple that rides on two rails. The ball screw drive is 98% efficient at converting rotational to linear motion, and allows a small Pittman GM9413-2 electrical motor to power the system. This motor provides a maximum continuous 45 oz-in of torque with 0.6 amperes of current and 65 rpm. The probe array pipe is connected to the drive system by a double-faced flange welded to its bottom. This flange has a full nipple above it and the 32-pin electrical feedthrough below it. A machined aluminum clamp holds the nipple to the rails. Above the nipple is a custom edge-welded bellows that keeps vacuum while allowing the array to move. This bellows has a compressed and extended length of 20 and 70cm, respectively, for a total travel of 50 centimeters. The pipe is preventing from rubbing against the vessel by a boron nitride sleeve bearing welded to the back of the vessel flange. This bearing also

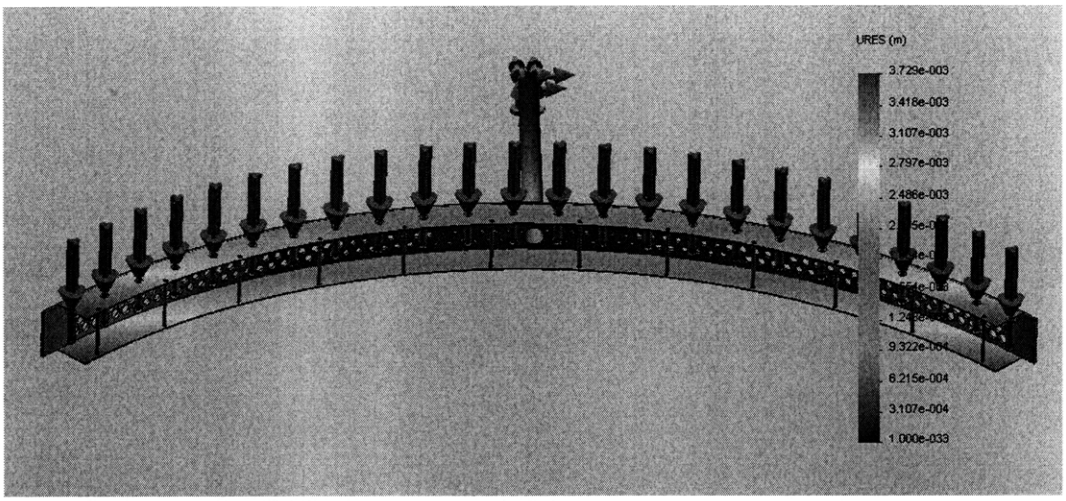

Figure 3-11: SolidWorks simulation of the probe array. Colors show the amount of deviation from a perfectly rigid model. Maximum deviation is 1.6mm.

relieves the torque put on the weld in holding the pipe upright. The entire assembly is mounted to the vessel by a large aluminum channel. This channel is screwed to gussets that are welded onto the vessel itself. Figure 3-12 illustrates how the various components of the drive system connect to each other.

Automation

The vertical position of the probe array is remotely controlled by a programmable logic controller (PLC) system. A Rockwell Automation/Allen Bradley MicroLogix 1500 PLC was installed at LDX prior to the probe array's construction, and was modified to control the probe array in addition to the other probes it controls. A 1769-HSC high-speed counter module was added to the PLC to count the pulses from an optical encoder and determine the array's position. The Dynapar M151000/8291A optical encoder sends 1000 pulses per revolution of the ball screw and has three channels of quadrature which allow the counter to count forward backward. The

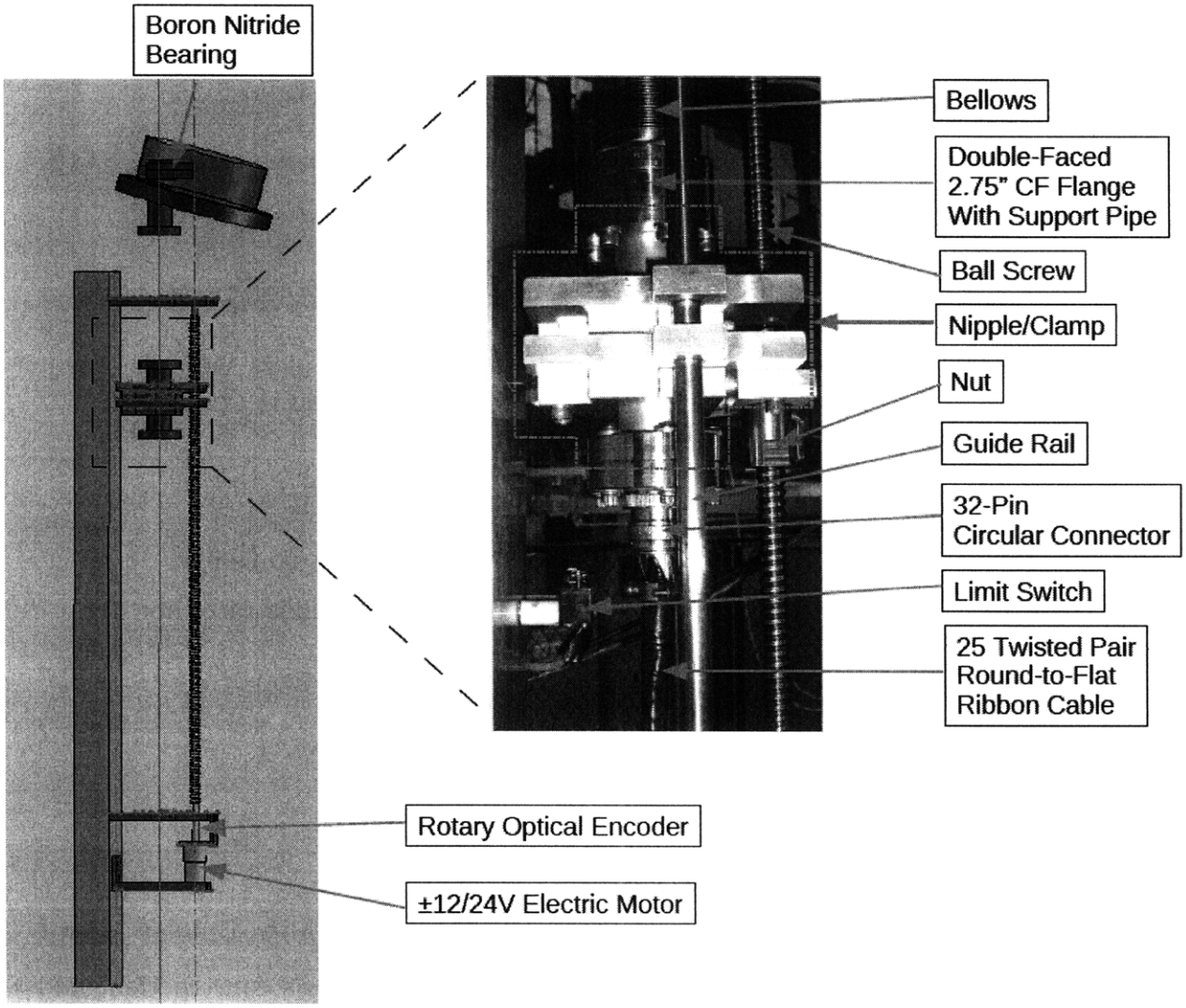

Figure 3-12: Diagram pointing out the various components of the probe array movement system.

PLC was programmed such that the last movement of the probe is always in the same direction. The ball screw has some backlash and always driving the probe in the same direction ensures that the probe tips are consistently positioned despite being withdrawn or inserted into the vessel. The constant direction is in, so when a withdraw signal is given to the PLC, it retracts the probes one centimeter past the target and drives them back in at half speed until the target is reached. The relay outputs on the PLC were all occupied, so an external relay box was constructed to handle the motor control logic. This allows the PLC to control the probes via low-current digital outputs.

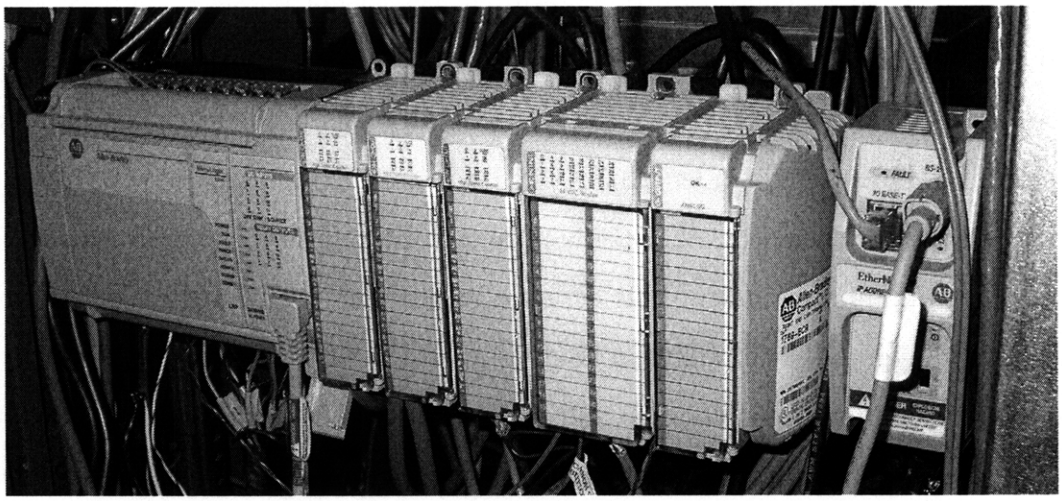

Figure 3-13: A picture of the programmable logic controller that controls the probe array movement system.

Materials

Since the array is an in-vacuum, plasma-facing component, it was required to be nonmagnetic and stainless steel. The field produced by the charging coil below the vessel reaches approximately 0.5 Tesla at the array location, and the force applied

to it from charging cycles could deform or fatigue the structure and cause it to become inaccurate or fail prematurely. Stainless steel also has a low vapor pressure and outgasses slowly compared to other materials, allowing a high vacuum to be maintained in the vessel. These criteria restricted the material choice to the 314 or 316 alloys of stainless steel. Alloy 316 was chosen due to its lower magnetic permeability and higher resistance to cold work magnetization.

The electrodes at the probe tips are 0.125 inch diameter, 2% thoriated tungsten. The electrodes are 3.5 inches in length, with 1 centimeter exposed at the tip. Their large size increases their heat loading capability and prevents the tips from melting during deep plasma penetration or high-intensity plasma bursts. The electrode is hard silver brazed to a solid copper conductor that runs the length of the ceramic insulator. Solid conductor was chosen since rigidity was needed in positioning and maintaining the exposed tip length.

The protective insulators that make up most of the probes themselves are 99.8% non-porous alumina ceramic. This ceramic was chosen for its high melting point, low gas trapping, and availability in many shapes and sizes. The terminal blocks are also made of high-alumina ceramic and 314 stainless steel. The electrical insulators at the base of the probe holders are made of the high temperature thermoplastic polyetheretherketone (PEEK), which is more suited to high vacuum applications compared to other plastics due to its low outgass rate, high melting point, and mechanical durability.

The in-vacuum wiring was done with 24 gauge enamel coated magnet wire. The terminal block connections are bare wire clamped in the terminal block. The feedthrough connections are soldered sockets slipped over the feedthrough pins. The solid probe conductors are soft tin soldered to the pushpin connectors.

The bearing immediately behind the vessel flange is made of boron nitride. Boron

nitride is chemically nonreactive, has a high melting point, and does not rely on water molecules for lubricity (like graphite). Therefore, it does not degrade the vacuum or contaminate the plasma and maintains lubricity under vacuum.

3.1.2 Electrical

3.1.3 Probes

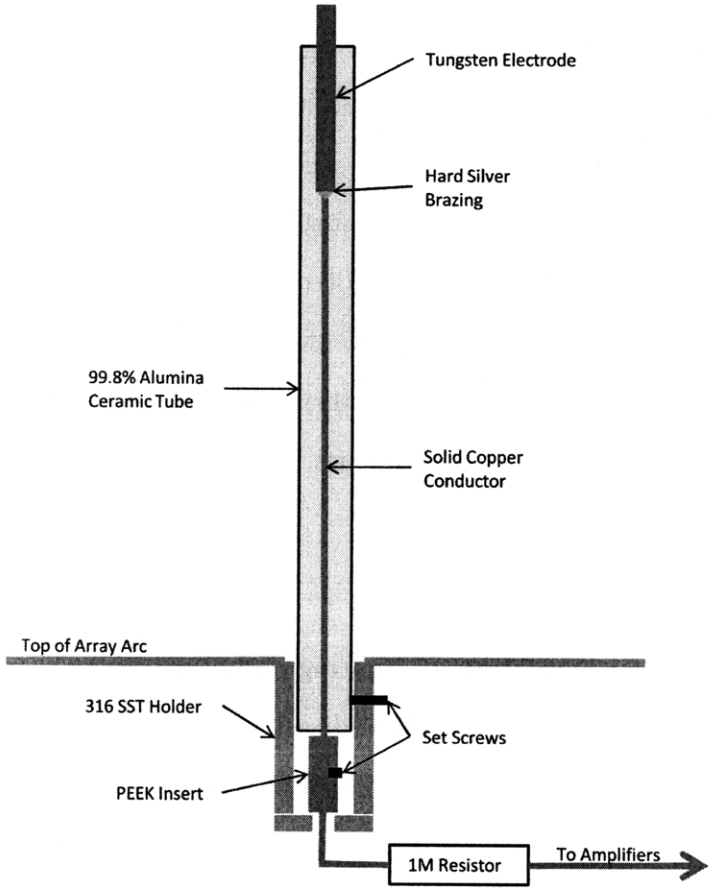

Figure 3-14: Diagram higlighting the various components of a single floating potential probe.

A diagram of a single probe is shown in figure 3-14. The tungsten electrode is not tight in the ceramic tube, and is held in place by the large solid copper conductor. This is done with two set screws, one that clamps the conductor to the PEEK insert below the ceramic, and on that clamps the ceramic to the steel holder. This way all probe components are secured to the array while maintaining the electrical isolation of the conductor.

Cabling

The signals are sent to the digitizers on shielded, 25 twisted pair, round-to-flat ribbon cable. Twisted pair was chosen to reduce pickup, and the single outer shield also helps reduce the external noise pick up by the cable run. The cable's round-to-flat feature made running it much easier since it wouldn't tangle and could pass through tight areas. The outer PVC jacket also protected against abrasion while running it. The ribbon style of the cable made the job of termination much simpler, faster, and less prone to faulty connections. Termination was done all at once with press-on, three-tier, 50 pin D-subminiature connectors.

Amplification

The electronics used for measuring the floating potential signals needed to be uniform across the channels since the signals are directly compared in the analysis. Gains are the most important since they directly affect the fluctuation magnitudes. The amplifiers are inverting and have a a gain of $g = -\frac{R_1}{R_2} = \frac{-10\text{k}}{1\text{M}+10\text{k}} = -0.0099$. They also have a 33pF capacitor in their feeback loops to prevent self-oscillation and give the amplifiers a -3db knee of $f_c = \frac{1}{2\pi R_2 C} = \frac{1}{2\pi(10e3)(33e-12)} = 482\text{kHz}$. This is well above the digitization frequency and the amplifiers start to alias well before an observed

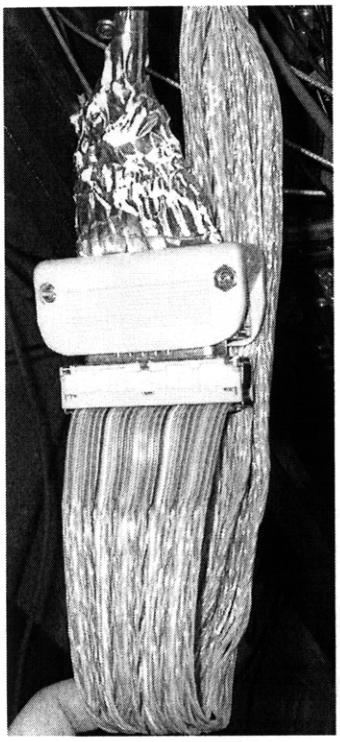

Figure 3-15: The signal cable showing the round-to-flat feature, twisted pairs, shielding, and termination.

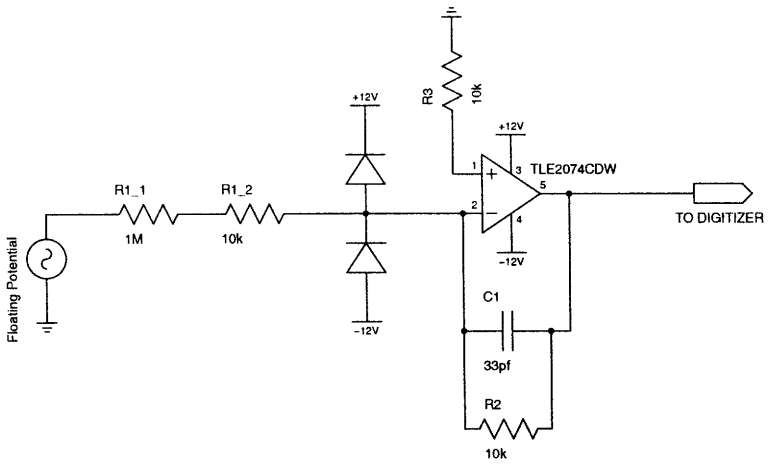

Figure 3-16: Schematic of the floating probe amplifiers.

signal attenuation from the amplification circuitry. The results of a SPICE simulation are shown in figure 3-17 and clearly show that the amplifiers have a flat frequency response until 480kHz. The measured frequency response of one channel is shown in figure 3-18 to closely agree with the simulation results. Expecting identical rolloff for every channel, testing each of the other gains only had to be done at one frequency. They were measured with an input signal of 10.5V at 10kHz. The results are shown in figure 3-19, and show a 3% maximum difference between any two channels.

The amplifiers we designed on custom printed circuit boards with quad amplifier chips. Quad amplifier chips were chosen in effort to keep the signal paths and operating conditions of every channel as close to identical as possible. Signal trace lengths were kept to a minimum with as few bends as possible to reduce pickup. The top and bottom traces were also not run on top of one another as to reduce parasitic

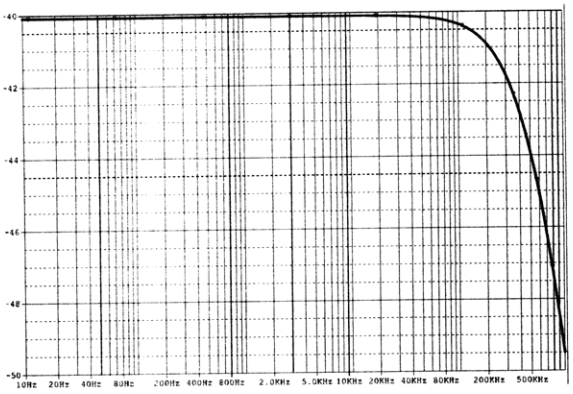

Figure 3-17: Spice simulation of an amplifier channel.

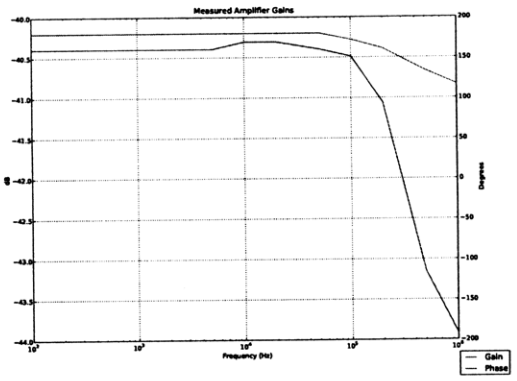

Figure 3-18: Measured gain and phase shift of channel 2.

capacitance. Each board has eight channels and its own positive and negative power supply regulators. Each amplifier chip also has 0.1uF ceramic decoupling capacitors connected at the chip's power pins. The entire system is powered by a remote switching power supply that resides in a shielded electronics rack on the main floor of the experiment. Power is sent to the amplifier box on a shielded three conductor cable terminated in a keyed circular connector. The enclosure also has a conducting braid gasket to to ensure uniform electrical connection between the lid and the case and helps shield out interference. The case is 1/8 inch die-cast aluminum, which also attenuates EMI better than a thin case.

Since the probes need to measure the floating potential, they need to draw as little current as possible while still being able to take and accurate measurement. A one megaohm resistor was placed in series with each probe, expecting that the plasma resistance is much lower than this value (as was shown in chapter 2). This resistor was placed as close to the probe tips as possible to minimize the probe capacitance and therefore keep the response time as fast as possible. The resistor is terminated into the virtual ground created by the operational amplifier shown in

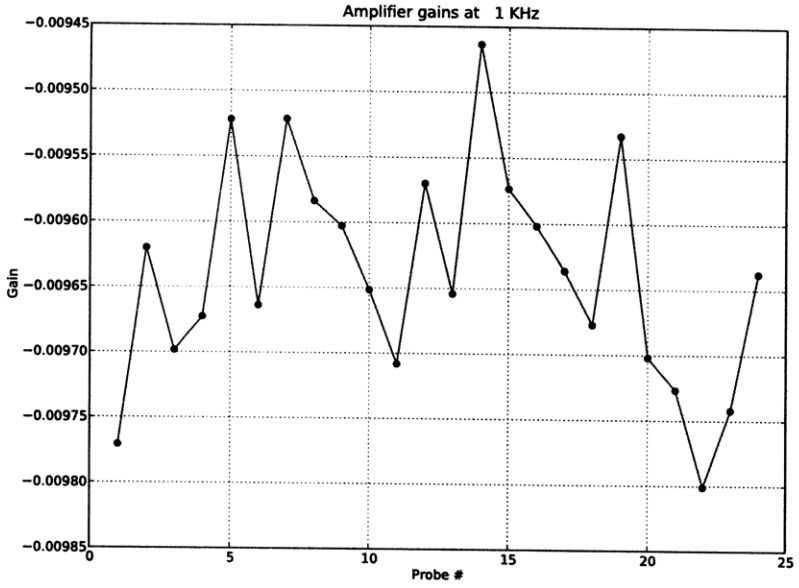

Figure 3-19: Probe gains at 1kHz

figure 3-16. The amplifier used is the Texas Instruments TLE2074CDW. It is a jfet-input amplifier with a 10MHz bandwidth-gain, 45 V/s slew rate, and $0.000025\mu A$ input bias current. The smaller, 10K resistor in series with the megaohm resistor resides on the amplifier boards, and protects the amplifiers in case of arcing to the conductor after the megaohm resistor. There are barrier diodes placed at the opamp inputs to shunt excess current to the power supply rails in case the input signal becomes so large as to pull the inverting input away from ground. This way, the digitizers are protected from excessive voltages.

The signal to noise ratio (SNR) is shown in figures 3-20 and 3-21. It was measured by comparing pre-plasma and plasma signals during shot 90311005. The lowest the SNR ever becomes is 40dB, showing that noise is not a problem in the probe electronics.

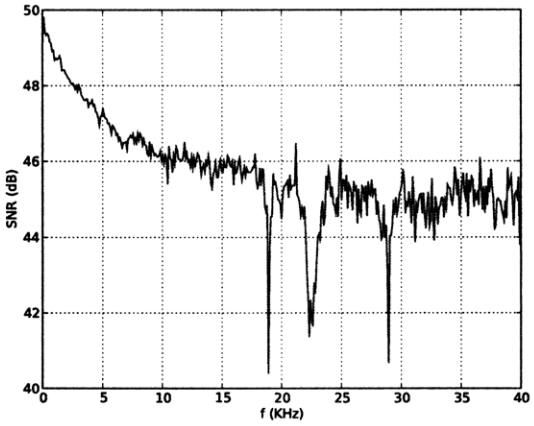

Figure 3-20: The signal to noise ratio from shot 90311005.

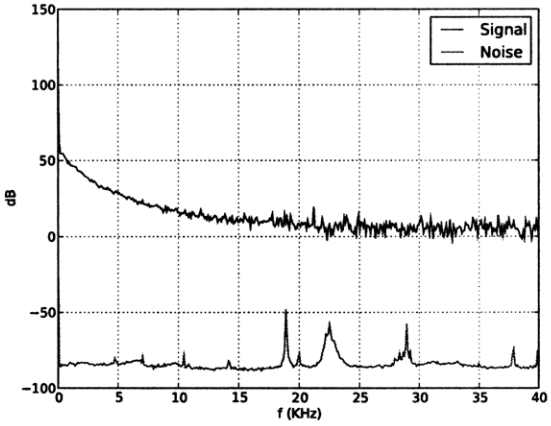

Figure 3-21: The signal and noise spectra from shot 90311005.

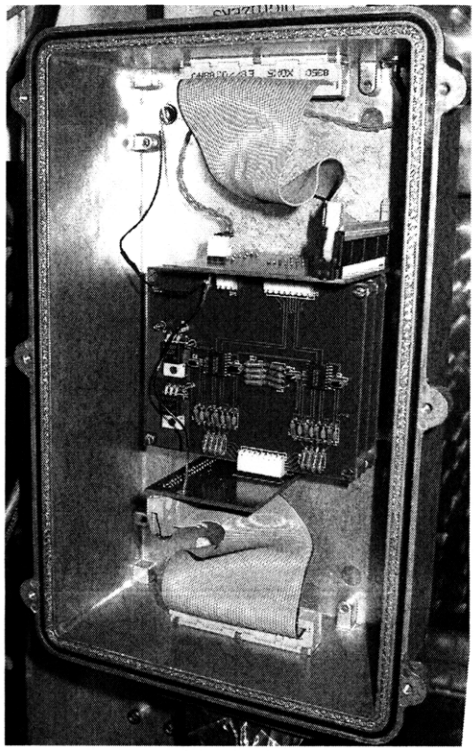

Figure 3-22: The amplifier box showing the amplifier stack, internal cabling, wall thickness, and electrical gasket.

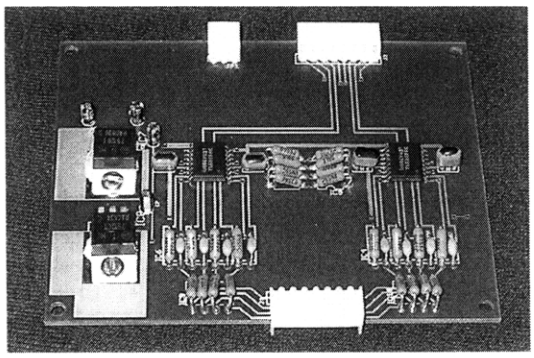

Figure 3-23: The top of the amplifier printed circuit board.

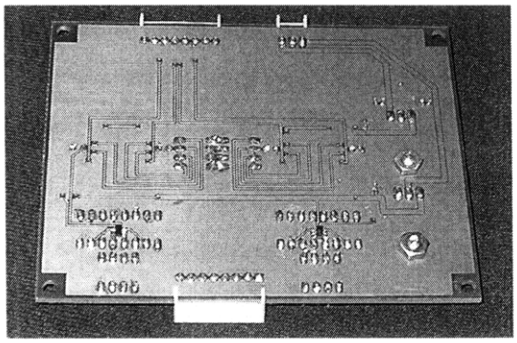

Figure 3-24: The bottom of the amplifier printed circuit board.

Digitization

Signal digitization is done by two INCAA Computers TR10 CompactPCI analog input boards. The TR10 is a 16-channel, 16-bit, bipolar digitizer with $\pm$10V fully differential inputs capable of 200kHz digitization and an onboard memory bank of 2 megasamples. Digitization was typically done at 80kHz, giving a record length of 25 seconds. Frequencies of interest are in the 10kHz range, making the 80kHz digitization rate well above the required Nyquist frequency.

There is a problem with the digitizers in that the 24 channels are spread across two digitizer cards, and these cards do not produce identical time stamps on the signals. This means there is a temporal jog in the data when looking between the signals from the two cards. It is apparent in the "stripey plot" show in figure 3-25. The lower 8 channels are lagging 11 data points behind the first 16 channels. This problem changed shot to shot so it had to be corrected by hand by direct inspection. The jogs appear to be normally distributed.

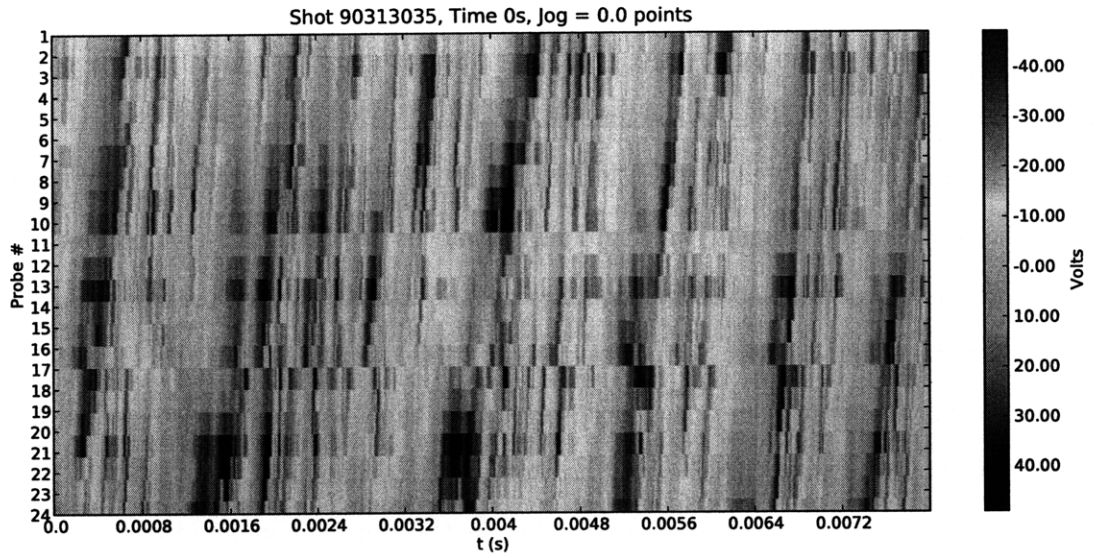

Figure 3-25: Stripey plot showing the jog in the data between the two digitizers. There is a clear dicontinuity between channels 16 and 17.

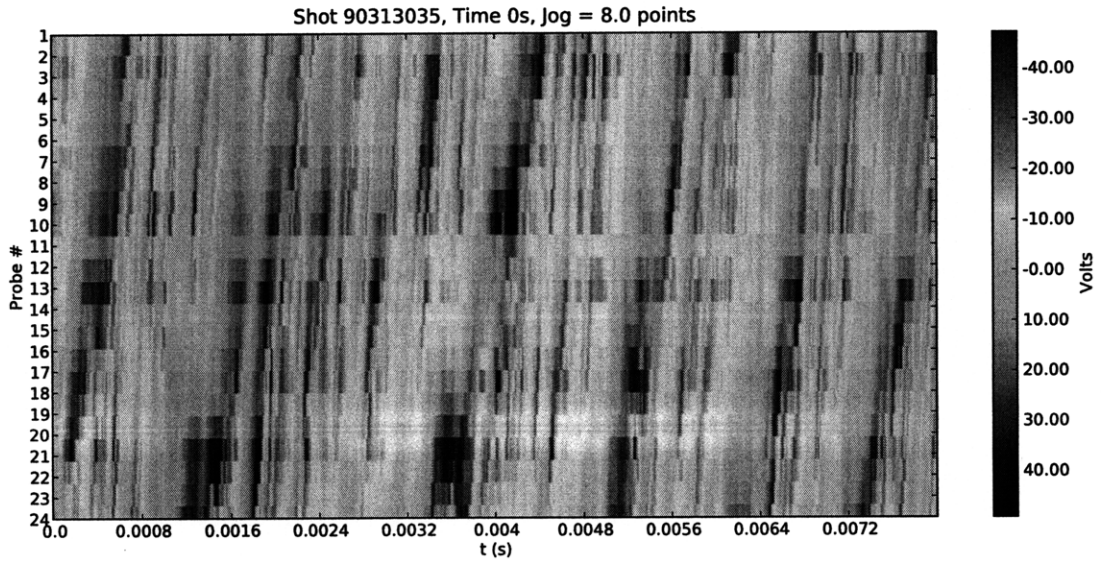

Figure 3-26: Stripey plot showing a jog corrected by shifting channels 17-24 by 8 data points.

Chapter 4

Experimental Observations

The data presented in this thesis came from LDX's October 2008, December 2008, and March 2009 runs. The runs each spanned three days, and produced hundreds of plasma shots. There usually are two or three lifts, or periods where the F-coil is levitated in between re-cooling, each day. The primary goal of the runs were to produce plasma conditions that allowed for observing fluctuations with a variety of conditions but with long enough periods of steady-state to be useful for statistical analysis such as presented in chapter 2.

In LDX, strong fluctuations are present at low gas pressures on the order of $10^{-6}\mu$Torr. As neutral gas pressure rises, the neutrals damp fluctuations via collisions and therefore fluctuation intensity typically decreases with neutral gas pressure. The gas pressure normally rises throughout a lift due to buildup of fueling gas, and therefore the first few shots of a lift are the ones that exhibit the strongest fluctuations. Fluctuations were first identified using a time spectrogram of probe 4 then analyzed with the bispectral method during different heating regimes and the afterglow.

A spectrogram is formally called a "time-frequency domain" plot, or TFD, and shows the frequencies present in a signal over a time interval. The spectrograms presented here were constructed by plotting the Fourier transform of 4096 data points from the input signal along the y-axis with color representative of intensity. The window was then shifted 512 points down the signal, and the Fourier transform was plotted on the y-axis again. This process was repeated until the entire signal was plotted.

Each of the RF heating sources can be turned on independently, and the heating sequence is shown underneath the spectrogram in the following results subsections. The afterglow is the time after all the heating sources have been turned off and the plasma is sustained by the confined particles. The initial spectrogram is good for picking up where interesting things happen since as the plasma rotates any spatial wave spectrum will be picked up in time as well. It is also quick to perform, thus allowing every shot to be briefly examined.

4.1 E x B Drift

An eight millisecond period from shot 81003019 is shown in figure 4-1. It is a "stripey plot," which is constructed by plotting each signal from the probe array side by side and representing the signal amplitude with color. This stripey plot is very similar to most of the shots taken and displays the features set out to examine here. Therefore, it is the only one reported. The computed average radial $E \times B$ drift velocity over this period is -0.11 millimeter per second. The instantaneous velocity, however, ranges from 34.7 km/s to -20.8 km/s, depending on position and time. The sound speed for cold ions and 25 eV electrons is $c_s = c\sqrt{T_e/m_i c^2} \cong 35\frac{\text{km}}{\text{s}}$ [10]. The $E \times B$ drift velocities have a near-zero mean are the same magnitude as the ion sound speed.

Having an average drift velocity close to zero is consistent with a convective flow type. It transports the same amount of particles in as it does out, just like a thermal convective cell.

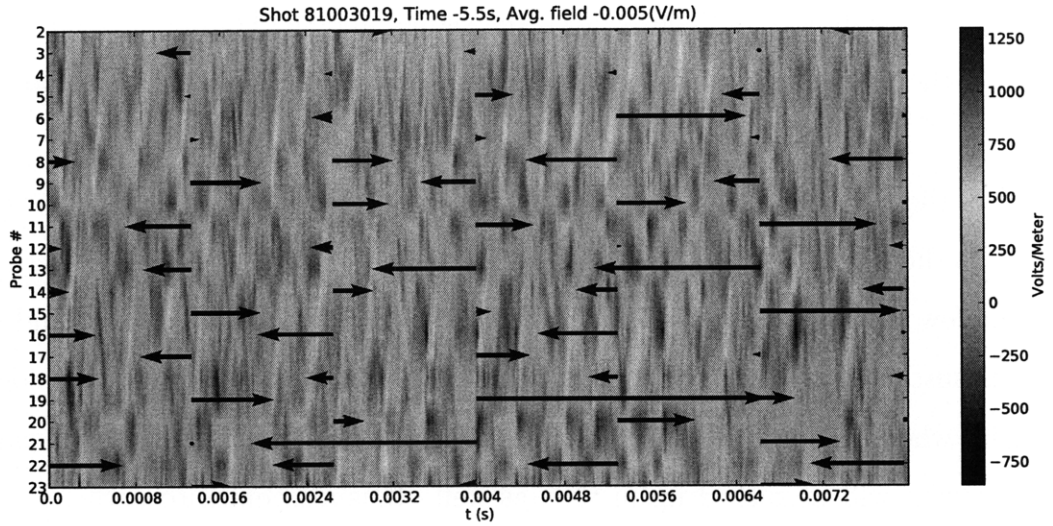

Figure 4-1: Stripey plot showing the electric field in color and the drift velociy as a vector field.

4.2 Fluctuation Phase Velocity

The fluctuation phase velocity is easily determined from a stripey plot. The slope of the lines on a stripey plot gives phase velocity per equation 2.28. Figure 4-2 shows the plasma rotating with a velocity of $\left(\frac{8\times10^5 \frac{\text{samples}}{\text{sec}}}{18\text{samples}}\right)(22\text{probes})\left(\frac{\pi}{46}\frac{\text{m}}{\text{probes}}\right) = 6678\frac{\text{m}}{\text{s}}$. The mode number can also be determined from the stripey plot by counting the number of samples in between the "stripes." In figure 4-2, there are 23 points between stripes on a single channel, giving the mode number $m = \frac{90°}{18\text{points}}\frac{\text{mode }\#}{360°}23\text{points} \approx 5$. The stripey plot also shows that the phase velocity is in the counter-clockwise direction

when looking down at the floating coil. The coil is dipole-up, so the phase velocity is in the electron diamagnetic drift direction. The source of the velocity is unclear, since the potential fluctuations can be caused by a flow of plasma across the array or by a wave propagating through the plasma. Whatever the source, the linear dispersion relations shown in the following subsection indicate that either the flow rotates at a constant velocity or that the waves have a constant propagation speed.

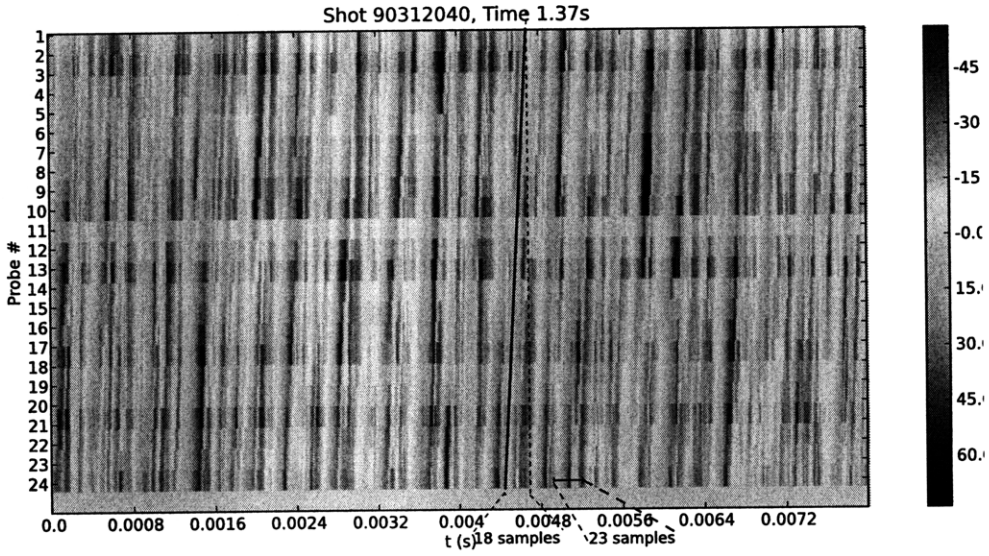

Figure 4-2: Stripey plot showing how the phase velocity is computed from the slope of the "stripes," and how the mode number can be determined from the distance between "stripes."

A trend appears when plotting the phase velocity against the neutral pressure measured on the vessel ion gauge. Figure 4-3 shows the data with a 5^{th} degree polynomial overlaid show the trends. Every shot plotted other than 90312015-90312024 were deuterium plasmas, and are the lower pressure shots. Shots 90312015-90312024 were helium plasmas, and are the higher pressure shots. There is a large increase in velocity around 5μTorr, which corresponds to the maximum density profile in LDX

[5] as shown by figure 4-4. The velocity decreases with pressure above 5μTorr, but there is another trend at lower pressures. The velocities lower than 5μTorr decrease and then increase again at lower pressures. This may be because the plasma density is not constant below 5μTorr, as seen in figure 4-4, and may give rise to a more complicated relation between neutral pressure and phase velocity. Above 5μTorr, the plasma density seems to be relatively constant, and the velocities decrease with neutral pressure as expected.

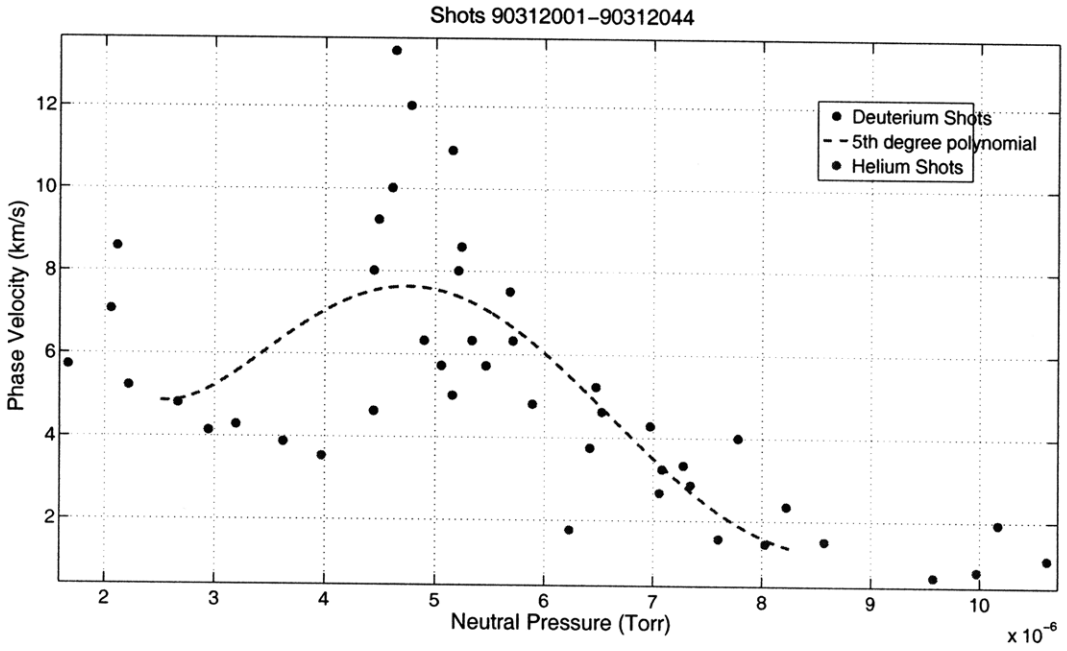

Figure 4-3: The plasma rotational velocity plotted against the vessel neutral pressure. There is a maximum at 5μTorr where the plasma density is greatest. Phase velocity decreases with neutral pressure when the plasma density is constant ($>$ 5μTorr). Below 5μTorr, the plasma density is not constant with neutral pressure, and the velocity/pressure relationship is unclear.

The general structure of the potential fluctuations also follow that predicted by simulations in a dipole field. Figure 4-5 shows the predicted structure of the poten-

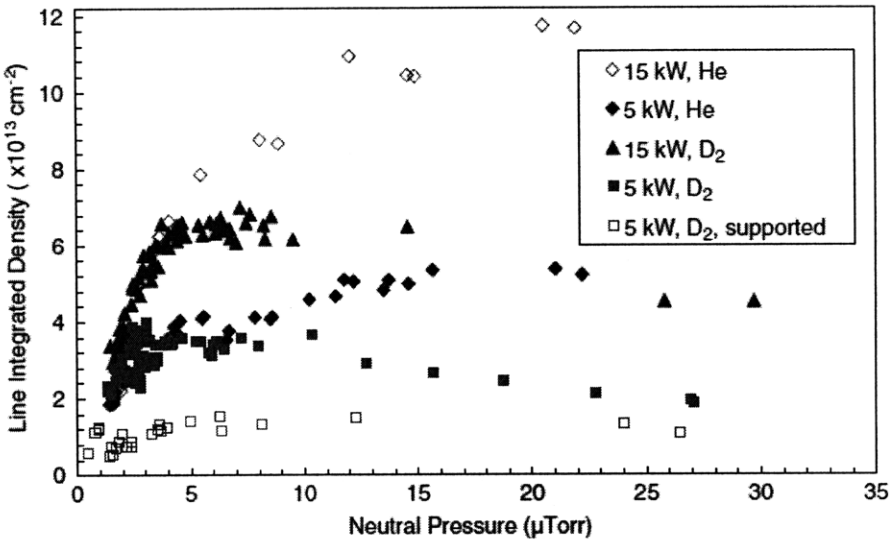

Figure 4-4: Plasma density vs. neutral pressure. Measured with the microwave interferometer on LDX.

tial fluctuations after the development of the Kelvin-Helmholtz instability where x is the radial direction and y is the azimuthal [14]. The outboard side of the fluctuations show large turbulent "blobs" that are azimuthally periodic. The stripey plots taken from the probe array clearly show constant, evenly spaced fluctuations in the azimuthal direction and could very well be turbulent blobs like those shown in figure 4-5.

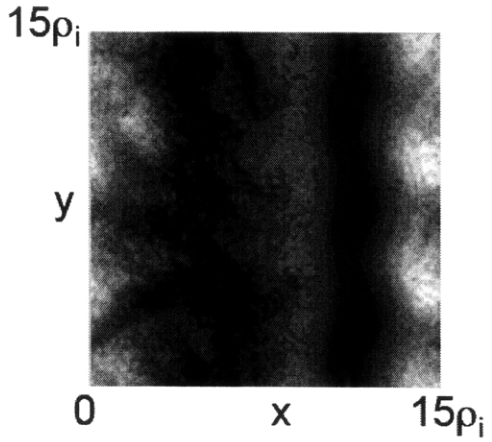

Figure 4-5: Potential structure results from a gyrokinetic simulation by Kobayashi in a dipole magnetic field after the Kelvin-Helmholtz instability is developed. [14] The "blobs" on the outer midplane (dimension x) have similar structure to the fluctuations measured by the probe array.

4.3 Bispectral Analysis

Since bispectral analysis is time consuming to process and understand, I have selected a few shots to illustrate the trends in the nonlinear coupling in LDX. The analysis must be performed over a 1 second period (80,000 time points) for the estimators to be well-converged. The self-consistent iterative solver often had stability problems and would cause the linear transfer function to grow a very large low wavenumber value within tens of iterations. However, there are several datasets that did result in convergent transfer coefficients, and convergence is a necessary condition for analysis validity. The spectrogram in the following shots have regions outlined in red where the transfer coefficient iteration diverges and regions outlined in green where it converges. The convergent results are shown in figures 4-6 through 4-11.

As an illustration, figures 4-17 and 4-18 show the results of a divergent time period before and after the linear transfer coefficient diverges. The before results are after 1 iteration so the quadratic term is subtracted out of the linear one. The diverged result are after 100 iterations. Figure 4-19 shows the result of analysis done in time at the same time interval as one of the spatial analysis.

Table 4.1: Summary of converged bispectral analysis results showing the heating and neutral pressure present during a time interval and whether or not the inverse energy cascade is observed.

Shot	Time	Heating	N. Pressure	Inv. Cascade
81003019	11.5 - 12.5	2.45	1.26 μTorr	yes
	14.8 - 15.8	afterglow	2.09 μTorr	no
81217011	0.5 - 1.5	2.45	0.66 μTorr	no
	15.5 - 16.5	afterglow	0.94 μTorr	no
80312025	0.9 - 1.9	2.45	1.86 μTorr	no
80312028	1.0 - 2.0	2.45	1.71 μTorr	no

4.3.1 Shot 81003019

This shot is from the October 2008 run, and is the last shot of the first lift. The initial vessel neutral pressure was 0.22 μTorr. During 11.5 to 12.5 seconds the vessel pressure steadily decreased from 1.26 to 1.17 μTorr, and during the 15.5 to 16.5 second period it steadily increased from 1.79 to 2.43 μTorr. The probe array was inserted to -52 centimeters from the midplane, which is 3 centimeters inside the approximate position of the separatrix at -55 centimeters. All three heating sources were used, as shown in figure 4-7. This style of heating is called a "wedding cake" shot since the plot of the heating looks like one due to the sources' staggered turn on and turn off times.

The convergence of the bispectrum estimator and the linear transfer coefficient are shown in figure 4-6. The convergence of the bispectrum was tracked by following a single, small wavenumber value and dividing it by the number of realizations at that point. The convergence of the linear transfer coefficient was done by tracking the sum of the entire coefficient. All of the convergence plots look very similar, so this is the only shot where it is explicitly shown. Notice that the only time which yielded a convergent result was during a heating period with 2.45GHz only and in the afterglow. An explaination for divergence in periods of strong heating is that the plasma is not changing slowly enough for the assumptions in the method to be valid.

The summed quadratic power transfer (lower left plot in figure 4-8) from 11.5 to 12.5 seconds show that high wavenumbers are quadratically damped and low wavenumbers are quadratically grown. The linear growth rate also shows a peak around the n=12 region. The linear growth rate is entirely negative, but this is a consistent result. The plasma has just gone through strong heating and the power has been decreased in this period. Therefore the plasma is relaxing despite being driven

with 2.45GHz. The afterglow region does not have any heating, so it is relaxing as well. Modes 1, 3, and 5 dominate this shot, as can be seen from the spatial spectrogram and the power spectra. The combination of high linearly excited wavenumbers, quadratic transfer from high to low wavenumbers, and low mode domination suggest that an inverse cascade of energy is occurring in this time interval. The results from the 14.5 to 15.8 period shown in figure 4-9 also show higher modes being excited, but the quadratic power transfer is negative for all modes. Mode 3 is dominant during this interval.

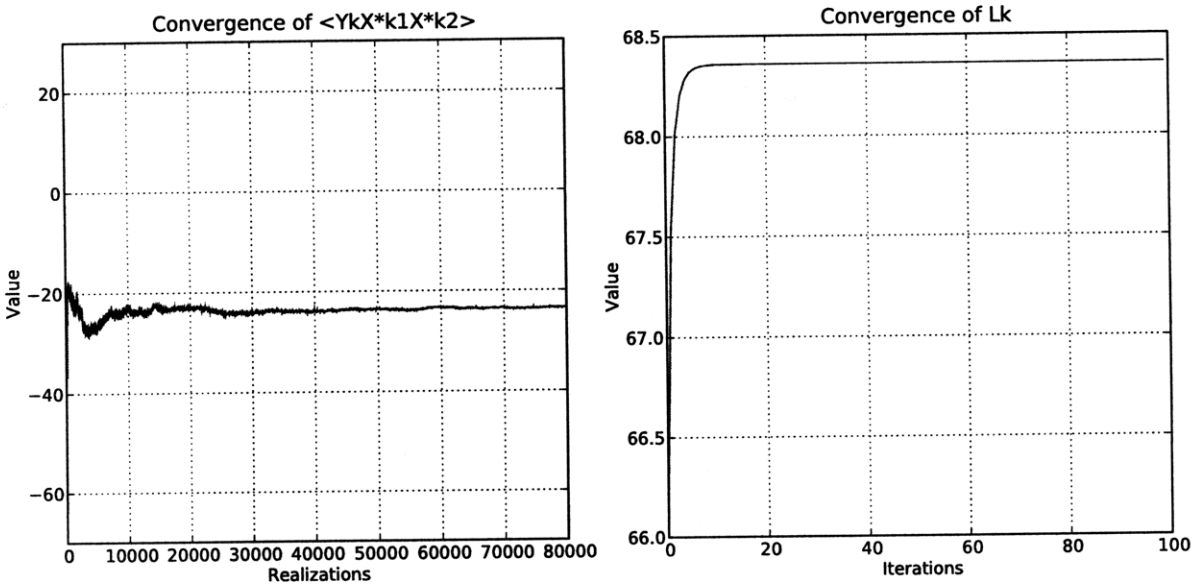

Figure 4-6: Convergence of the bispectrum and Lk in shot 81003019 from 11.5 to 12.5s. The bispectrum appears converged since 40,000 data points, and L_k converges after 10 iterations. Iterative solving for L_k does not change its value by much, either.

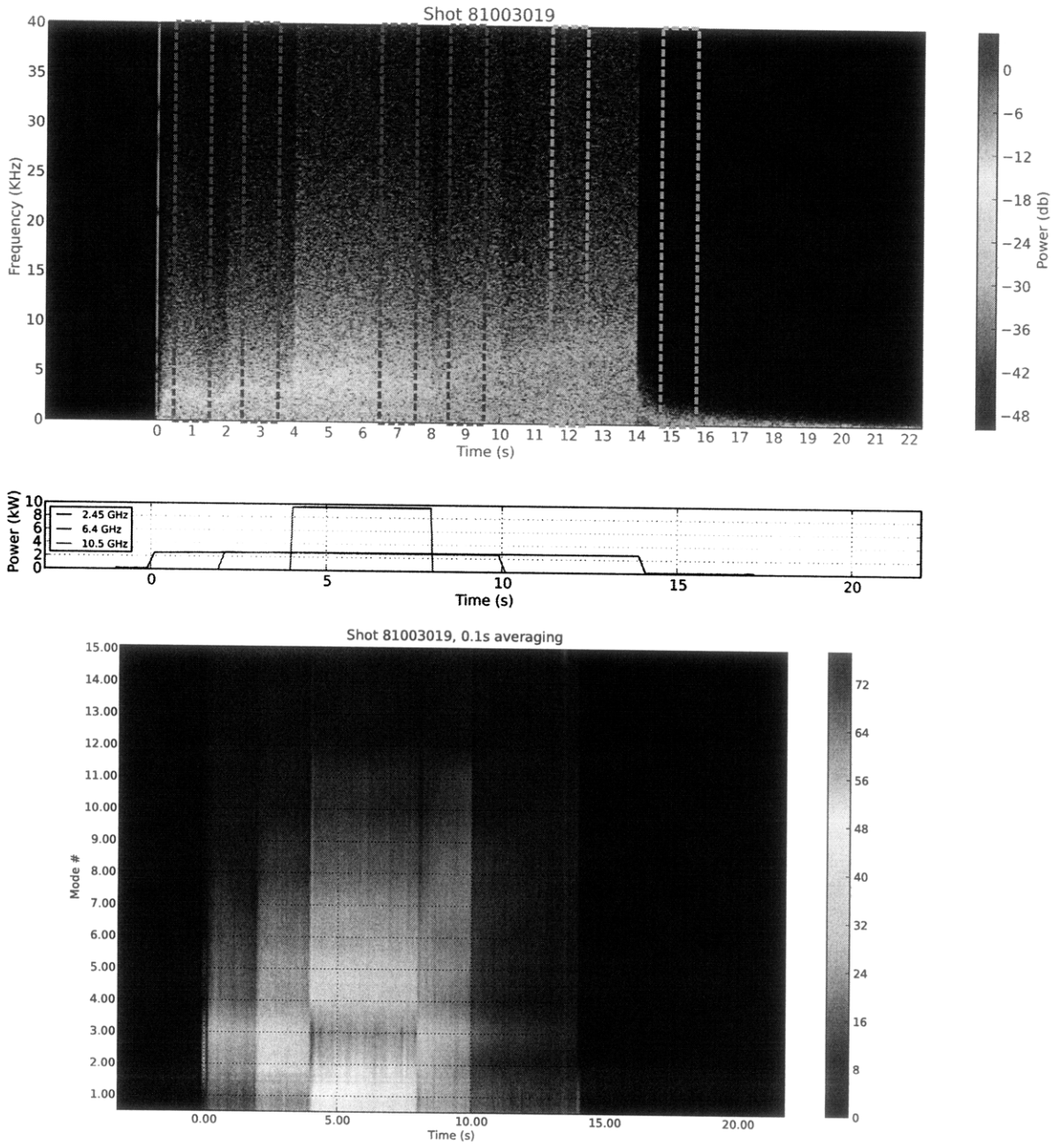

Figure 4-7: Temporal and spatial spectrograms of shot 81003019. Six time intervals were analyzed in this shot, and two intervals produced convergent results. The temporal spectrogram shows quasi-coherent modes in the 2-5KHz region, and little power above 10 kHz. The spatial spectrogram shows that the n=3 mode is dominant through most of the shot.

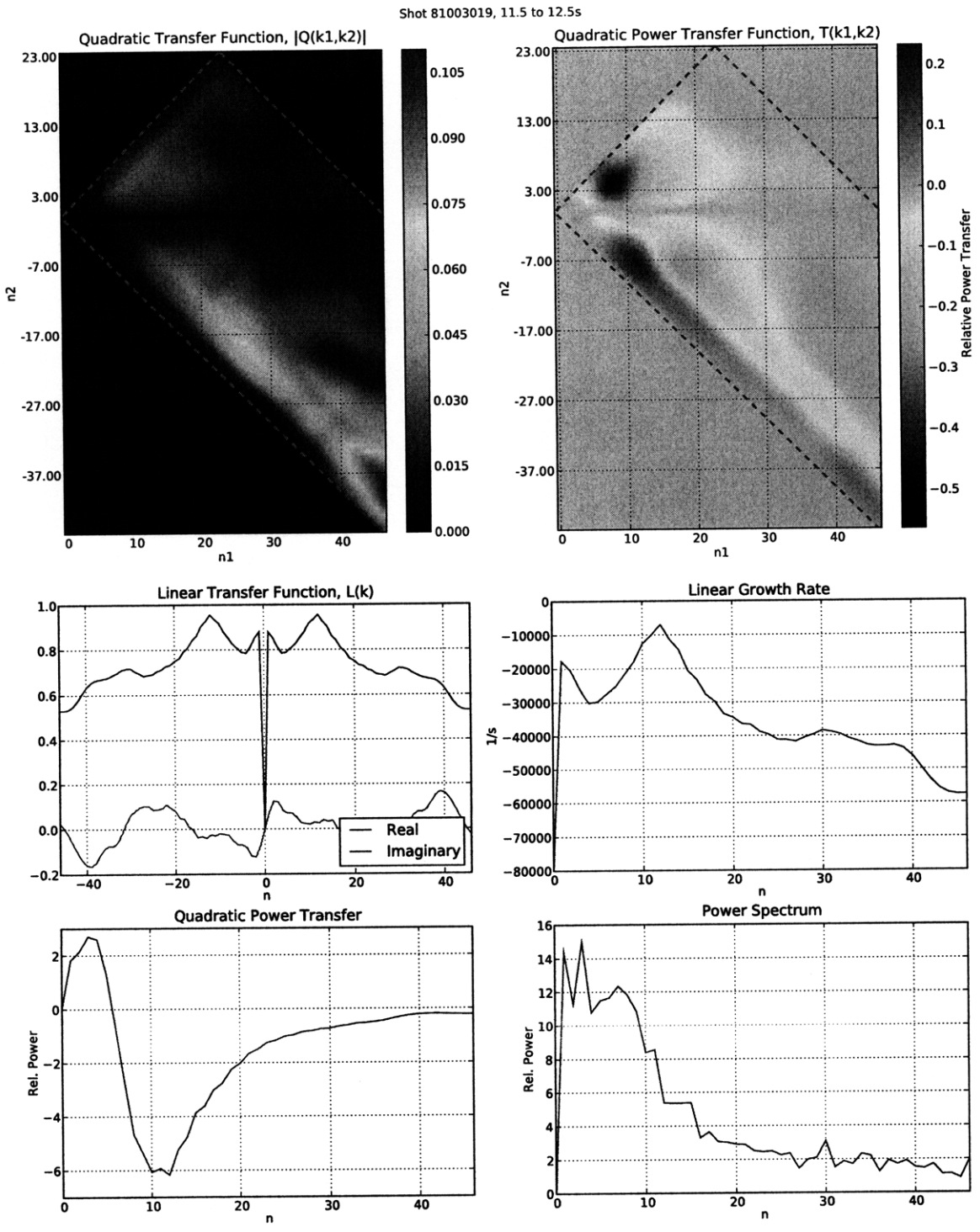

Figure 4-8: Spatial analysis during 11.5 to 12.5 seconds in shot 81003019. The quadratic power transfer shows that the inverse energy cascade is present, and the linear growth rate is least damped at modes where the quadratic power transfer is most negative. Modes 1 and 3 are dominant in the spectrum.

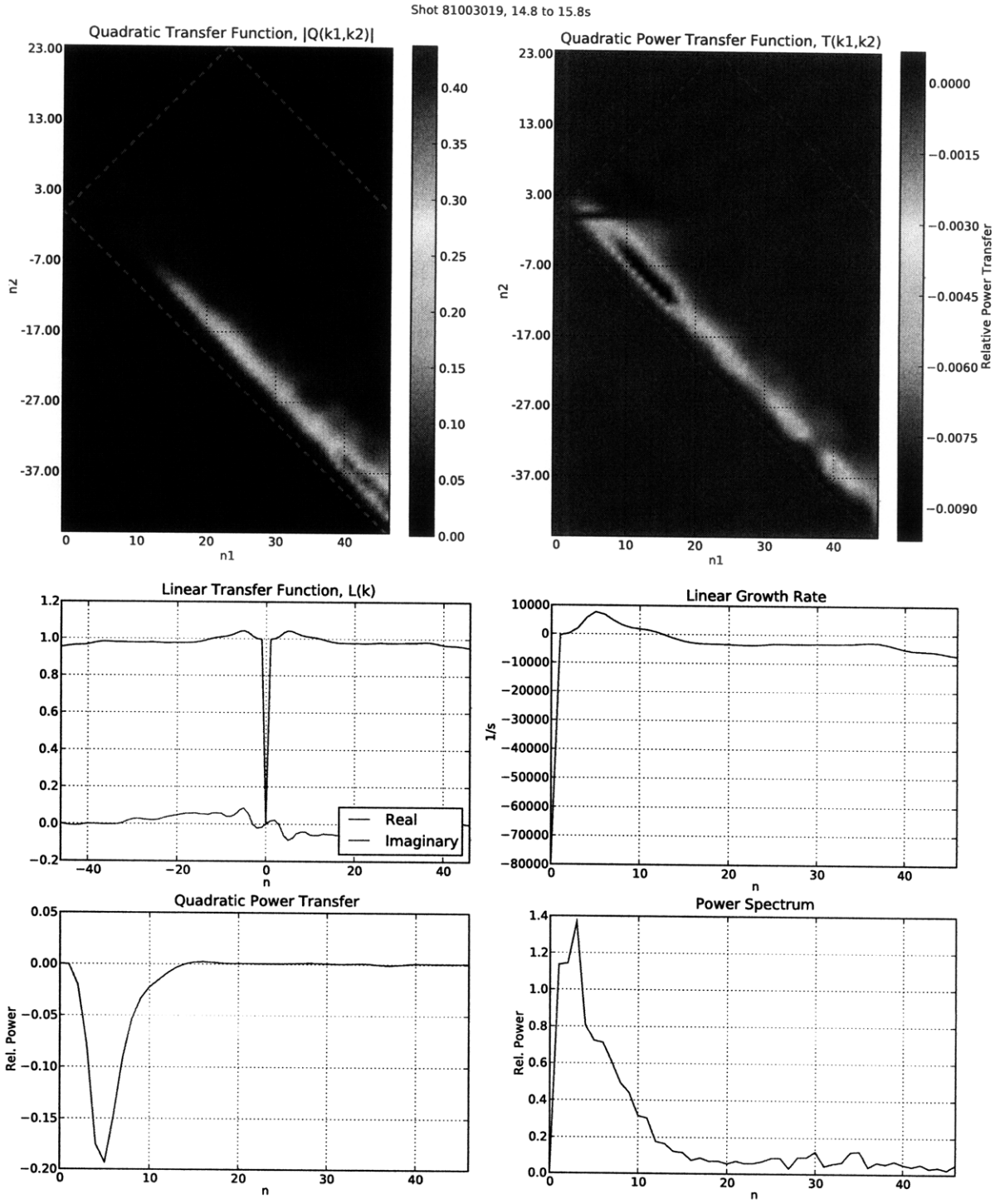

Figure 4-9: Spatial analysis during 14.8 to 15.8 seconds in shot 81003019. The quadratic power transfer shows that all modes are damped, and the linear growth rate is least damped at modes where the quadratic power transfer is most negative. Mode 3 is dominant in the spectrum.

4.3.2 Shot 81217011

This shot is one from the first day of the December run, and is the eleventh shot of the single lift that day. The initial vessel pressure was 0.34 μTorr. During 0.5 to 1.5 seconds the vessel pressure was a relatively constant 0.66 μTorr, and during the 15.5 to 16.5 second period it steadily increased from 0.93 to 0.96 μTorr. The probe array was inserted to -55 centimeters from the midplane, which the approximate position of the separatrix. All three heating sources were used, as shown in figure 4-7. Like shot 81003019, the "wedding cake" style of heating was used. The spatial spectrogram is plotted from .3 seconds onward since the initial mode was so strong that it threw the scale off. The only convergent periods were in the first 2.45GHz region and in the afterglow.

Both time periods in this shot show quadratic damping of low modes, but there is some quadratic growth in modes 12 to 21 during 15.5 to 16.5 seconds. This is the opposite effect the quadratic term had in shot 90312019. The earlier time period's spectrum is peaked at the first mode, and shows a very linear dispersion relation up to about n=10. The linear growth rate is entirely negative, but is peaked at low mode numbers. Again, this is a consistent result since the plasma is relaxing from the intial burst before 0.3 seconds, and then after the heating in the afterglow. The later time period is also peaked at n=1, but has positive linear growth from n=2 to 9. This is curious since the most energy is in n=1, but is neither quadratically or the linearly grown. The dispersion relation is also very linear, but only to around n=5 in this period.

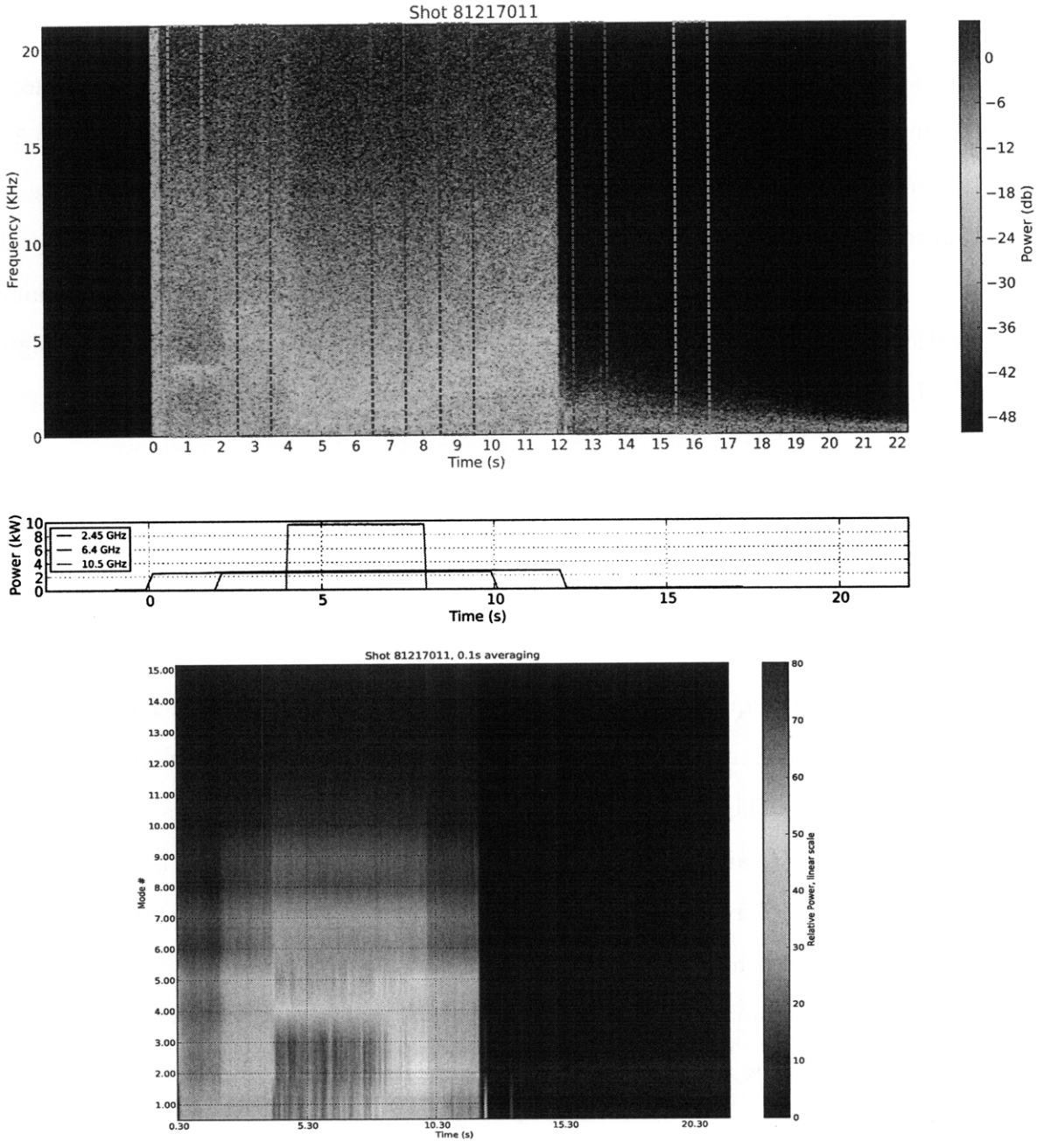

Figure 4-10: Temporal and spatial spectrograms of shot 81217011. The temporal spectrogram shows an initial wideband burst until 0.3 seconds, followed by a coherent mode. There are more coherent, but lower frequency modes during the higher heating periods. The spatial spectrogram shows that modes 1 and 3 are dominant.

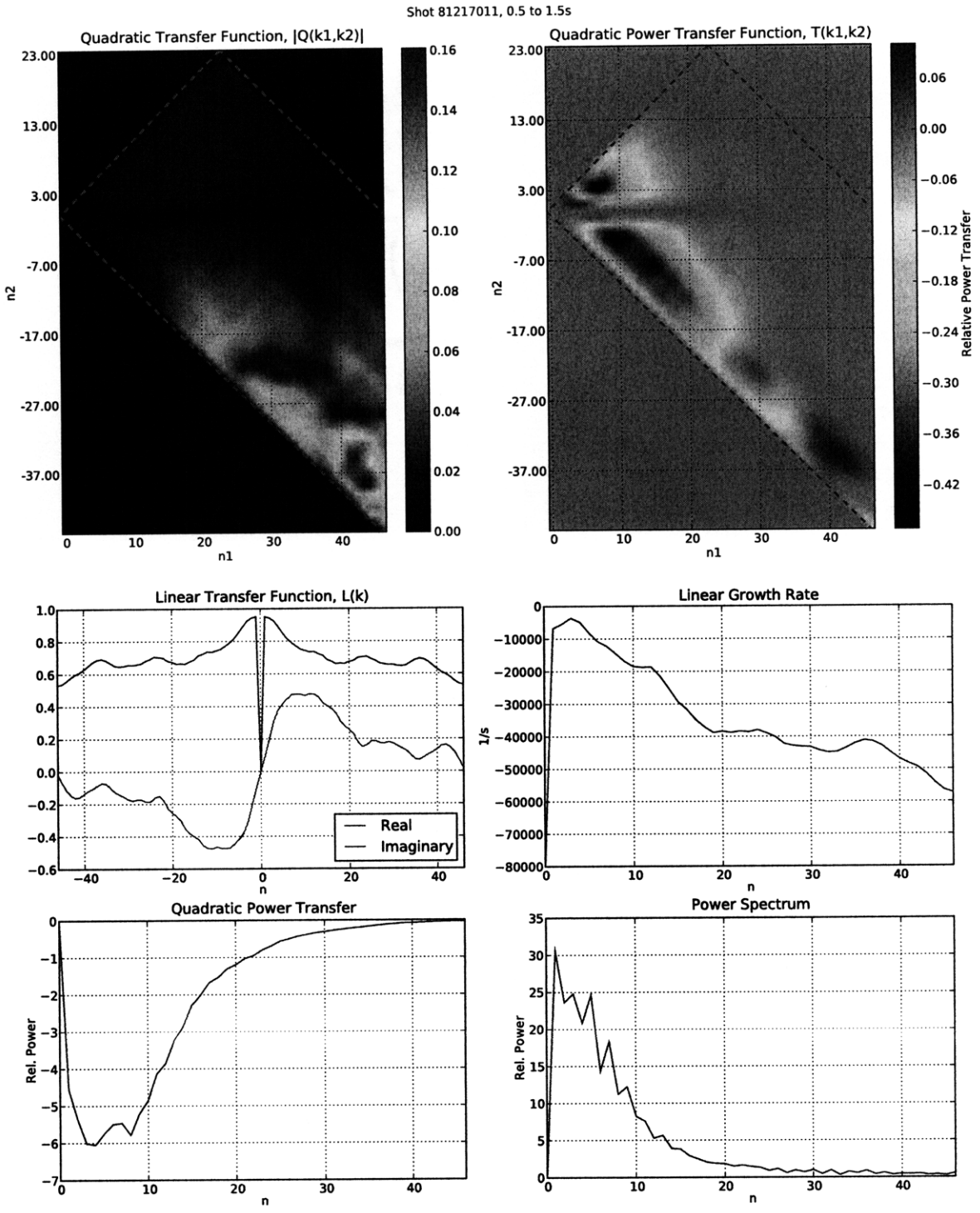

Figure 4-11: Spatial analysis during 0.5 to 1.5 seconds in shot 81217011. The quadratic power transfer shows that all modes are damped, and the linear growth rate is least damped at modes where the quadratic power transfer is most negative. Mode 1 is dominant in the spectrum. The dispersion relation is very linear to about n=10.

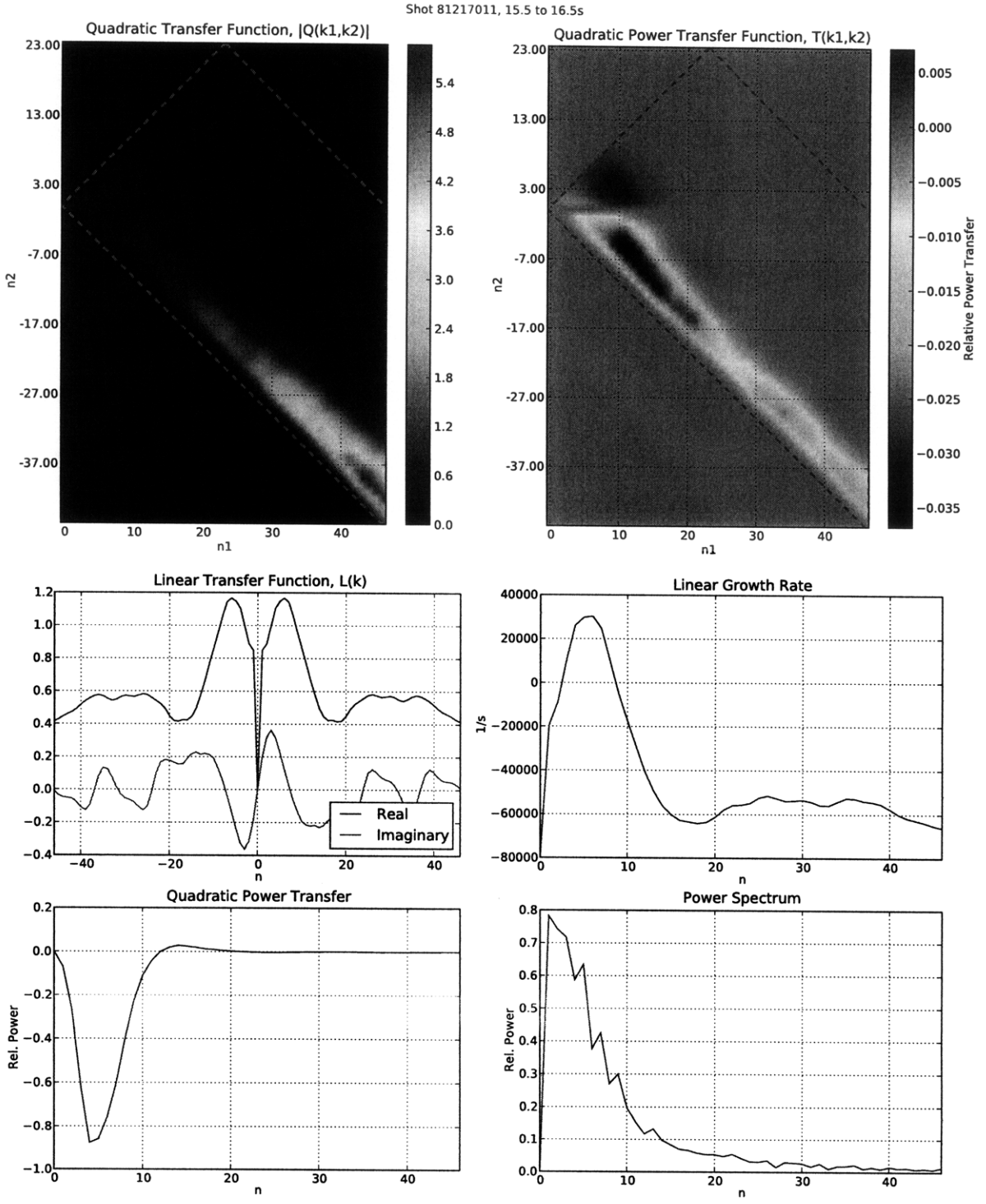

Figure 4-12: Spatial analysis during 15.5 to 16.5 seconds in shot 81217011. The quadratic power transfer shows that all low modes are damped, and n=12 to 21 are slightly grown. The linear growth rate is least damped at modes where the quadratic power transfer is most negative again. Mode 1 is dominant in the spectrum.

4.3.3 Shot 90312025

This shot is from the second day of the March run, and is the first shot of the third lift that day. The initial vessel pressure was 1.77 μTorr, and steadily rises from 1.83 to 1.91 μTorr during the period where the analysis was done. The probe array was positioned at -60 cm, further withdrawn than the previous two shots. All three heating sources were used with staggered start times, as shown in figure 4-13, but were all turned off after 10 seconds. This is the "truncated wedding cake" style of heating. The only period where the bispectral analysis converges is in the first 2.45GHz region.

It shows strong modes in all three heating regimes which can be seen in the time spectrogram in Figure 4-13. The spatial spectrogram in figure 4-13 also shows the time evolution of the spatial modes. It clearly shows that modes 1 and 3 are the dominant modes in this shot. There was only one period that produced a convergent result, and it shows linearly grown modes of n=3 to 6, and quadratically grown modes of n=7 and 8. The linear growth rate is positive in this time period because there was no initial burst and this is the first period of heating, so the plasma is building up. The quadratic and linear transfer coefficients appear to resemble a forward energy cascade where low modes are grown linearly and their energy is transferred to higher modes quadratically. The dispersion relation is linear to n=8.

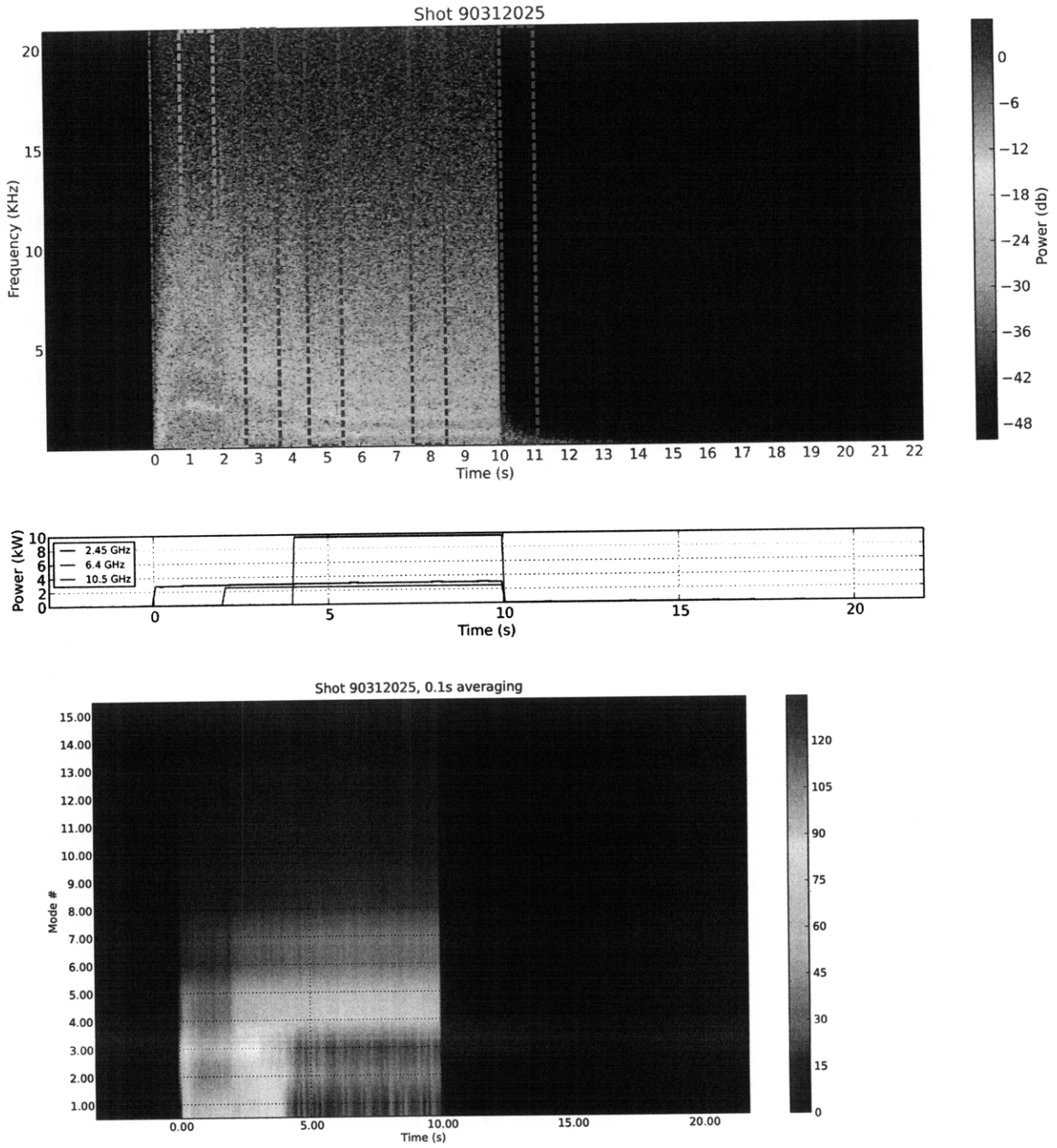

Figure 4-13: Time and spatial spectrograms of shot 90312025. The temporal spectrogram shows strong coherent modes throughout the shot, and the spatial spectrogram shows modes 1 and 3 are dominant.

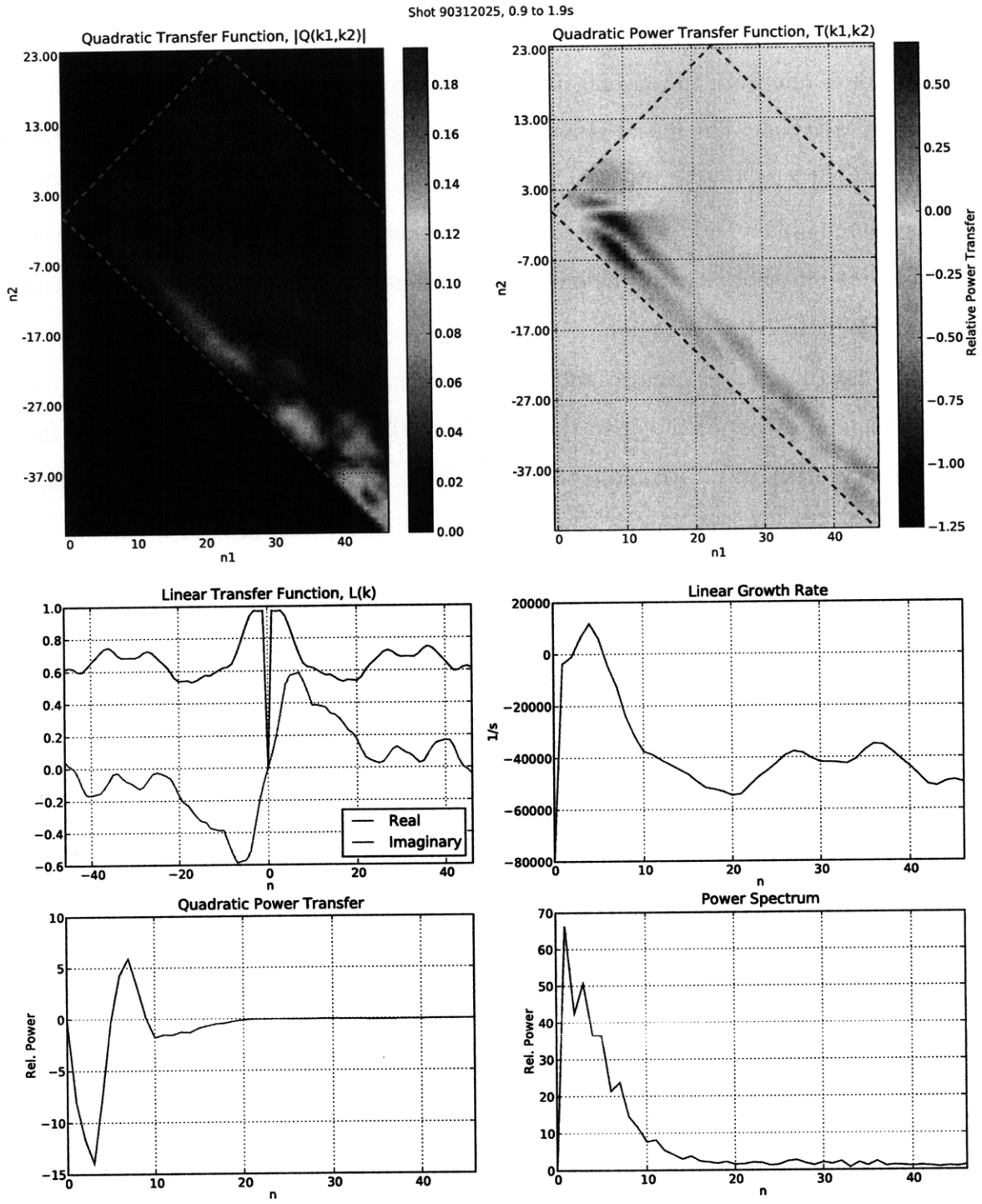

Figure 4-14: Spatial analysis during 0.9 to 1.9 seconds in shot 90312025. The quadratic power transfer shows that all modes other than 7 and 8 are damped, and the linear growth rate is least damped at modes where the quadratic power transfer is most negative. Mode 1 is dominant in the spectrum. The dispersion relation is very linear to about n=8.

4.3.4 Shot 90312028

This shot is one from the second day of the March run, and is the first shot of the third lift that day. The initial vessel pressure was 1.71 μTorr and steadily increased from 1.6 to 1.74 μTorr during the 1 to 2s period. The probe array was still -60 cm below the midplane, and was heated in the "truncated wedding cake" style, as it was in the previous shot. Again, the only period where the bispectral analysis converges was in the first 2.45GHz region.

The heating, gas pressures, and spectrograms, and dominant modes (n=3,5) in this shot are almost identical to those in shot 90312025, but is very different from it in every other way. All modes are linearly damped, but the growth rate has a large peak at n=1 and several more gradual, smaller peaks around n=27, 36, and 43. All modes are quadratically damped as well (no cascades at all), the low modes having the strongest negative summed power transfer. The linear transfer coefficient is rather chaotic after n=3.

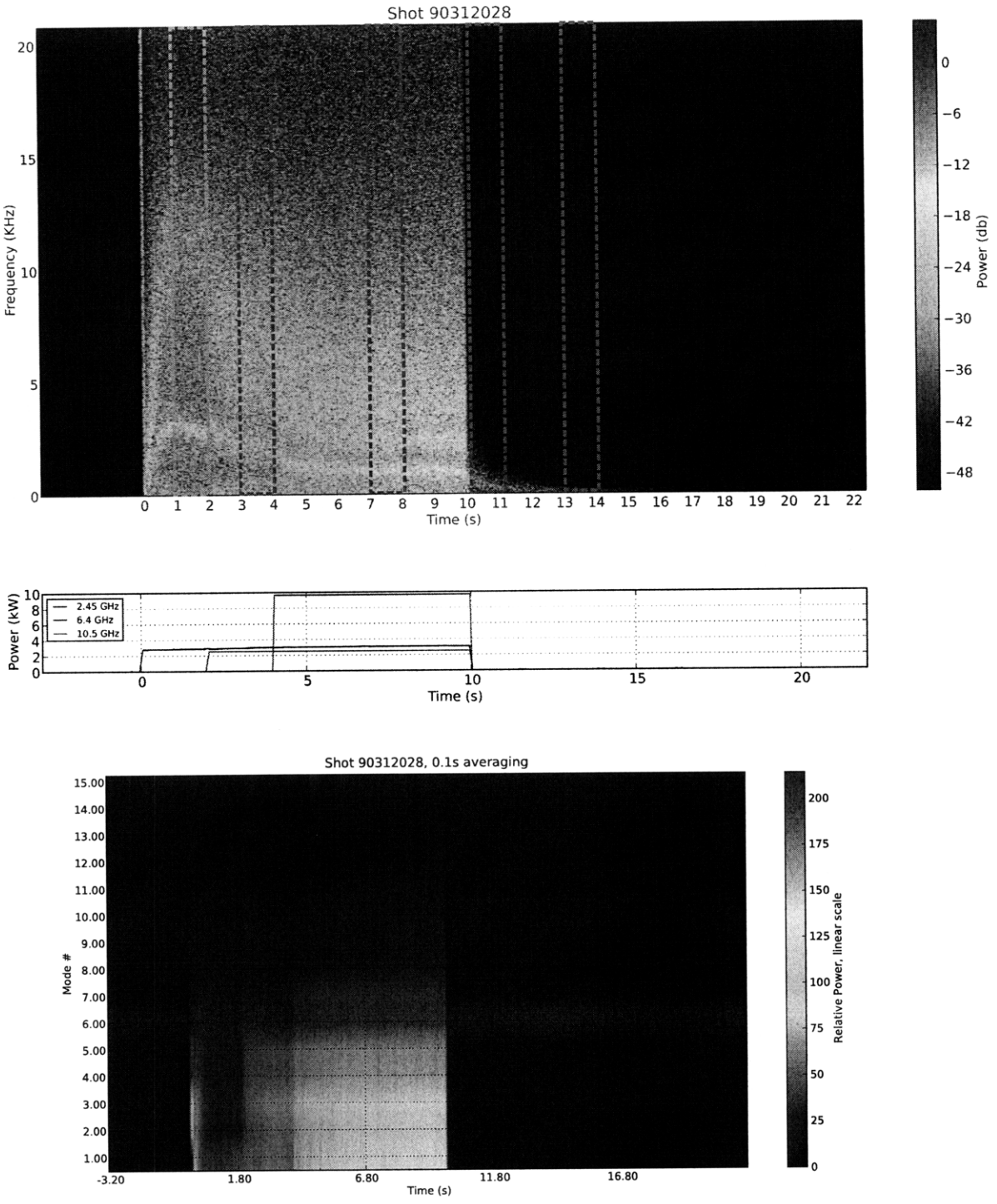

Figure 4-15: Temporal and spatial spectrograms of shot 90312028. Both show identical characteristics to shot 90312025 except that modes 1 and 3 are not quite as strong in the spatial spectrogram.

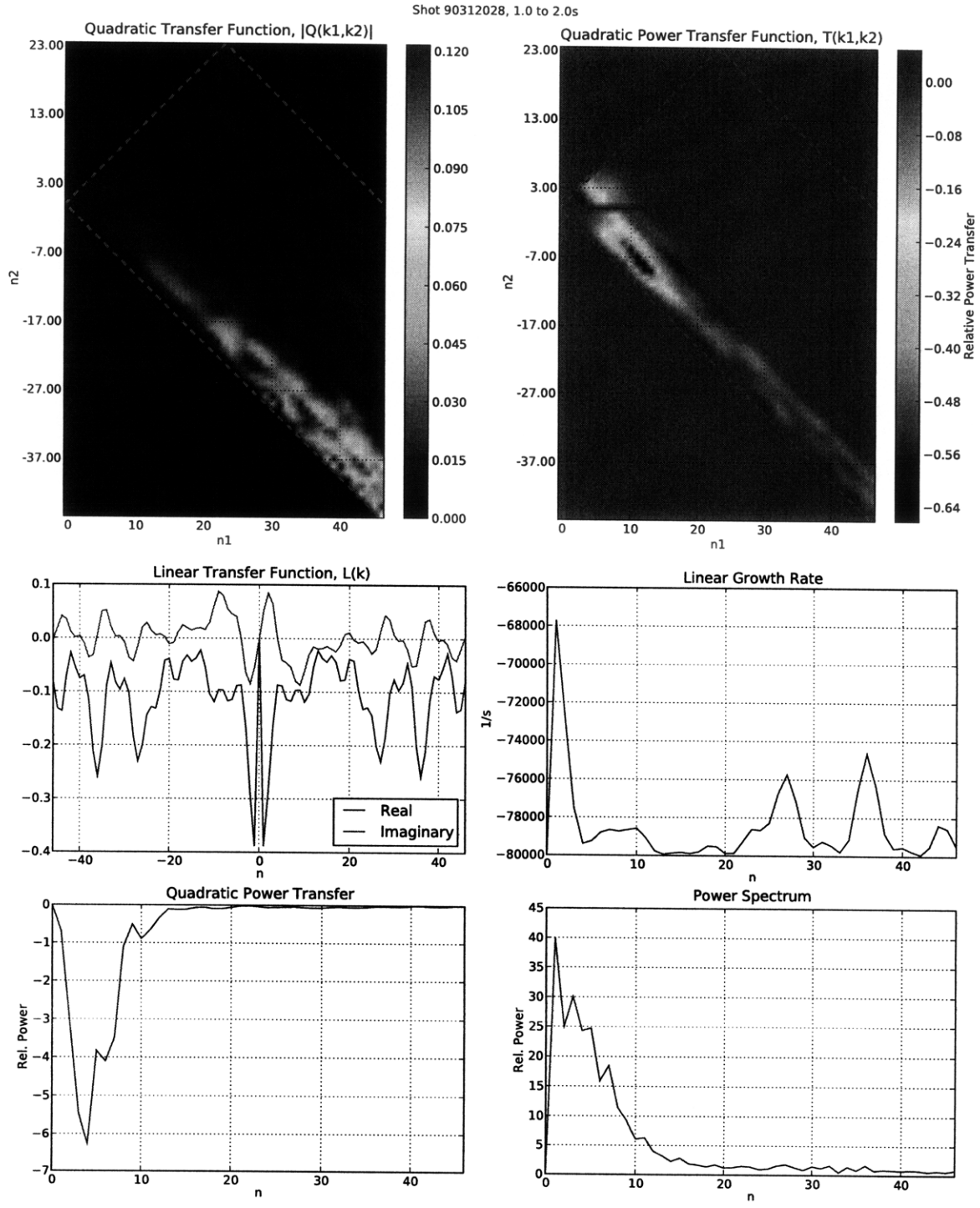

Figure 4-16: Spatial analysis during 1 to 2 seconds in shot 90312028. The quadratic power transfer shows that all modes are damped, and the linear growth rate is least damped at m=1. The linear growth rate also has some high mode spikes. Mode 1 is dominant in the spectrum. The dispersion relation is only linear to about n=3.

4.3.5 Divergent Analysis

It is worthwhile to mention the characteristics of the analysis in a divergent case, if simply for completeness. The results from 2.5 to 3.5s in shot 81003019 are shown after 1 solver iteration in figure 4-17 and after 20 iterations in 4-18. Performing one iteration subtracts the quadratic transfer coefficient out of the linear coefficient (the 0^{th} iteration guesses $Q_k = 0$), and would be the closest guess to an accurate solution in a divergent case (assuming the estimators are well-converged).

Notice that it is qualitatively similar to the convergent results from 11.5 to 12.5 seconds in the same shot. This may mean that the first iteration is close to the real result but is numerically unstable. Its divergence makes the results untrustworthy, nonetheless, unless they are proven to be close in the future by comparison to convergent analysis during the same time period. The large low mode that is grown in both transfer coefficients after several iterations can clearly be seen in figure 4-18. It dominates the plots and no other features can be seen.

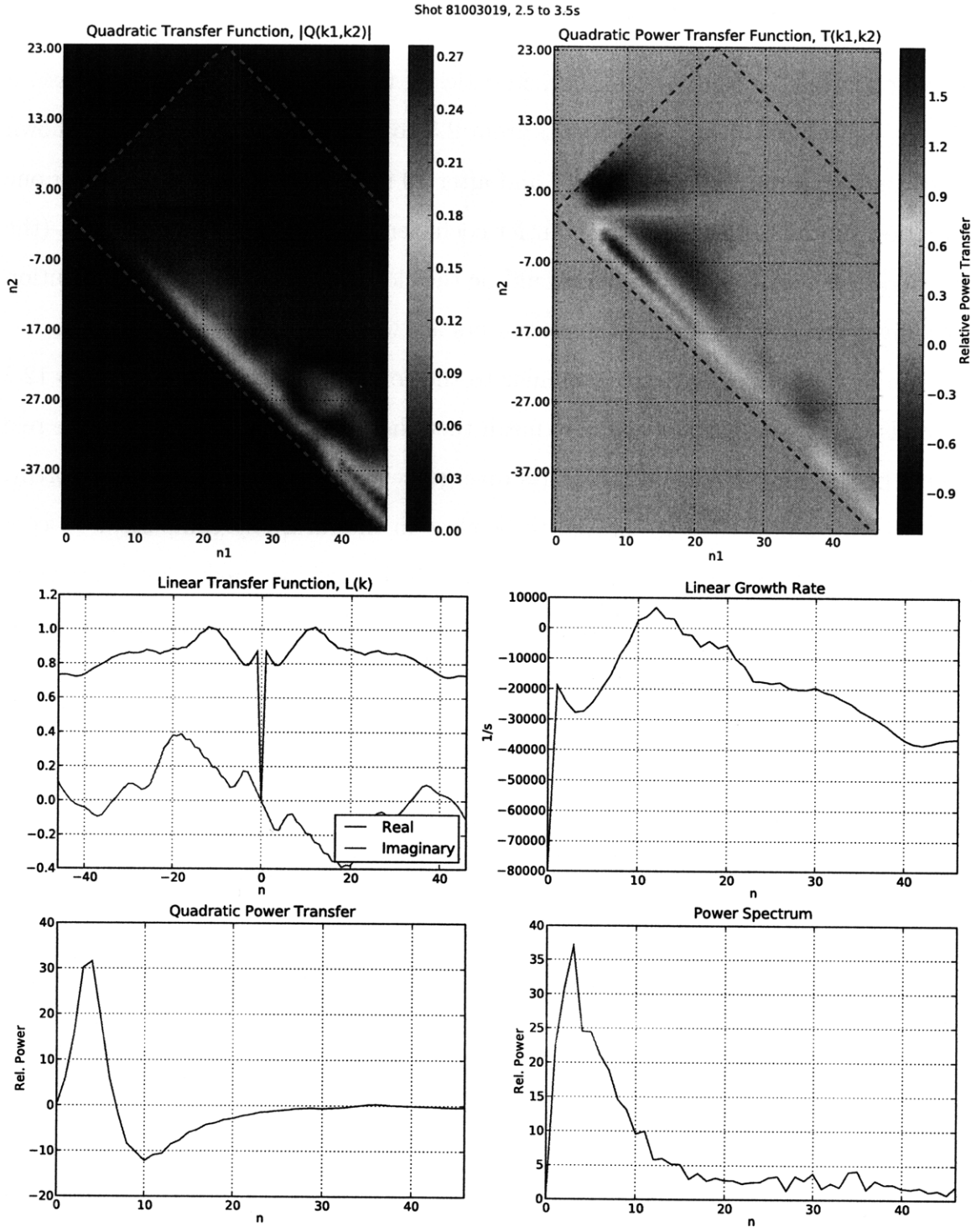

Figure 4-17: Divergent results after one iteration.

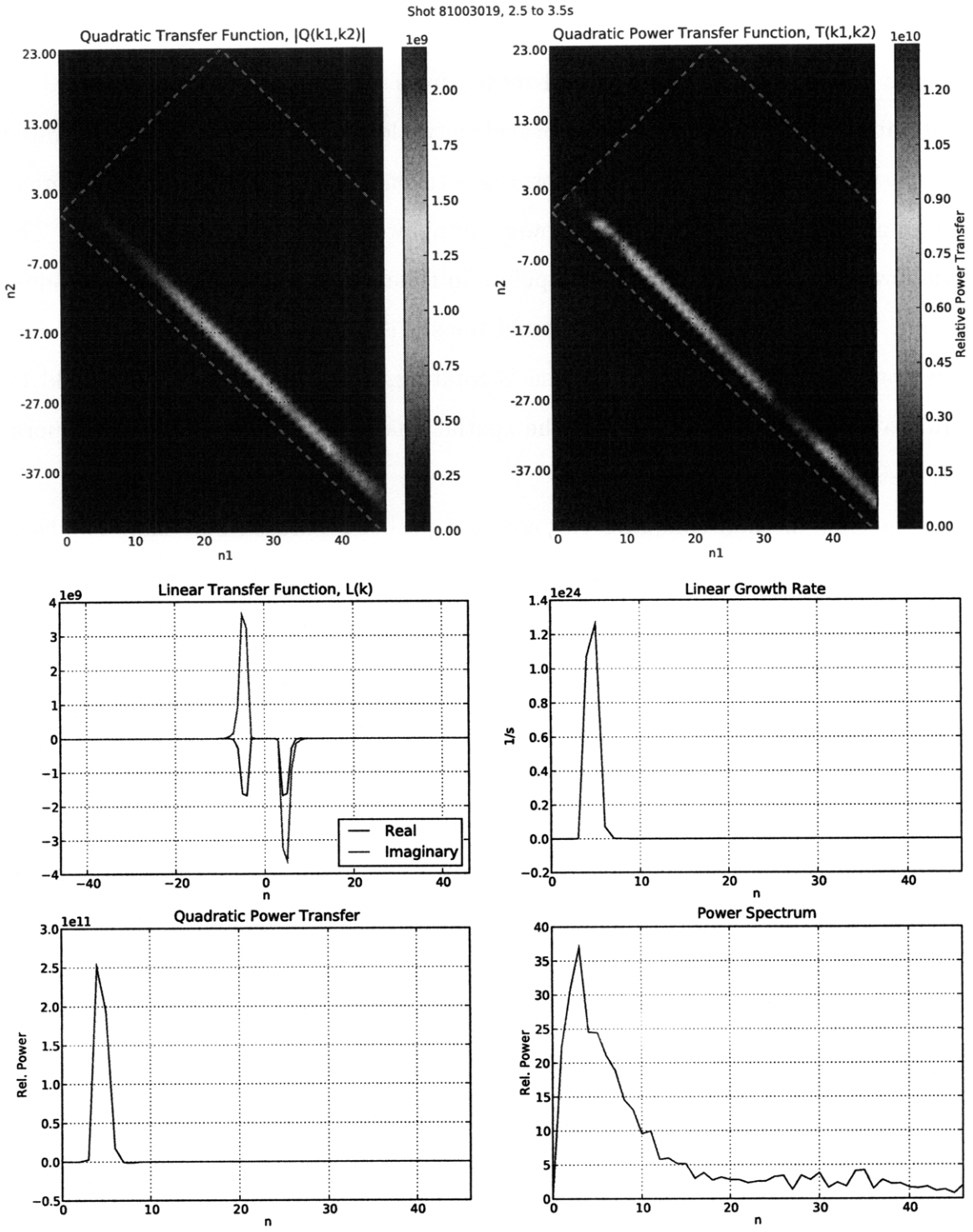

Figure 4-18: Divergent results after twenty iterations.

4.3.6 Time Analysis

Figure 4-19 shows the time method results from 2.5 to 3.5s in shot 81003019. To reiterate, the analysis in time is performed on two long time signals that are seperated in space. Short time Fourier transforms are taken from the two signals at identical times and their bispectrum, crosspower, autopower, et cetera, are computed. The window is shifted down a few data points in time and the quantities are computed again. This is done many times to build the statistical estimators used to calculate the transfer functions. If the plasma is rotating, any spatial structures should be translated into time signals, and the spatial analysis should match the temporal analysis.

The time method compares two adjacent probes separated by 7 cm. The close spacing of the two probes increases the correlation of the signals measured from them, but also reduces the magnitudes of the estimators compared to those computed spatially. All of the plots look qualitatively similar to the spatial results of the same time interval in the single iteration plot in 4-17. They both show an inverse energy cascade to low modes, similar power spectra, and a linear dispersion relations until n=20. The spatial analysis has a different linear growth rate shape that show only higher modes being linearly excited. The temporal analysis shows strongest linear excitation for low modes. Unfortunately, they are also both similar in that they are divergent. I was unable to get any time analysis to converge even for time periods that were convergent in the spatial case. The agreement between spatial and temporal bispectral analysis supports the observations made by Grierson, and validates the use of a two-point temporal method to study the characteristics of spatial modes.

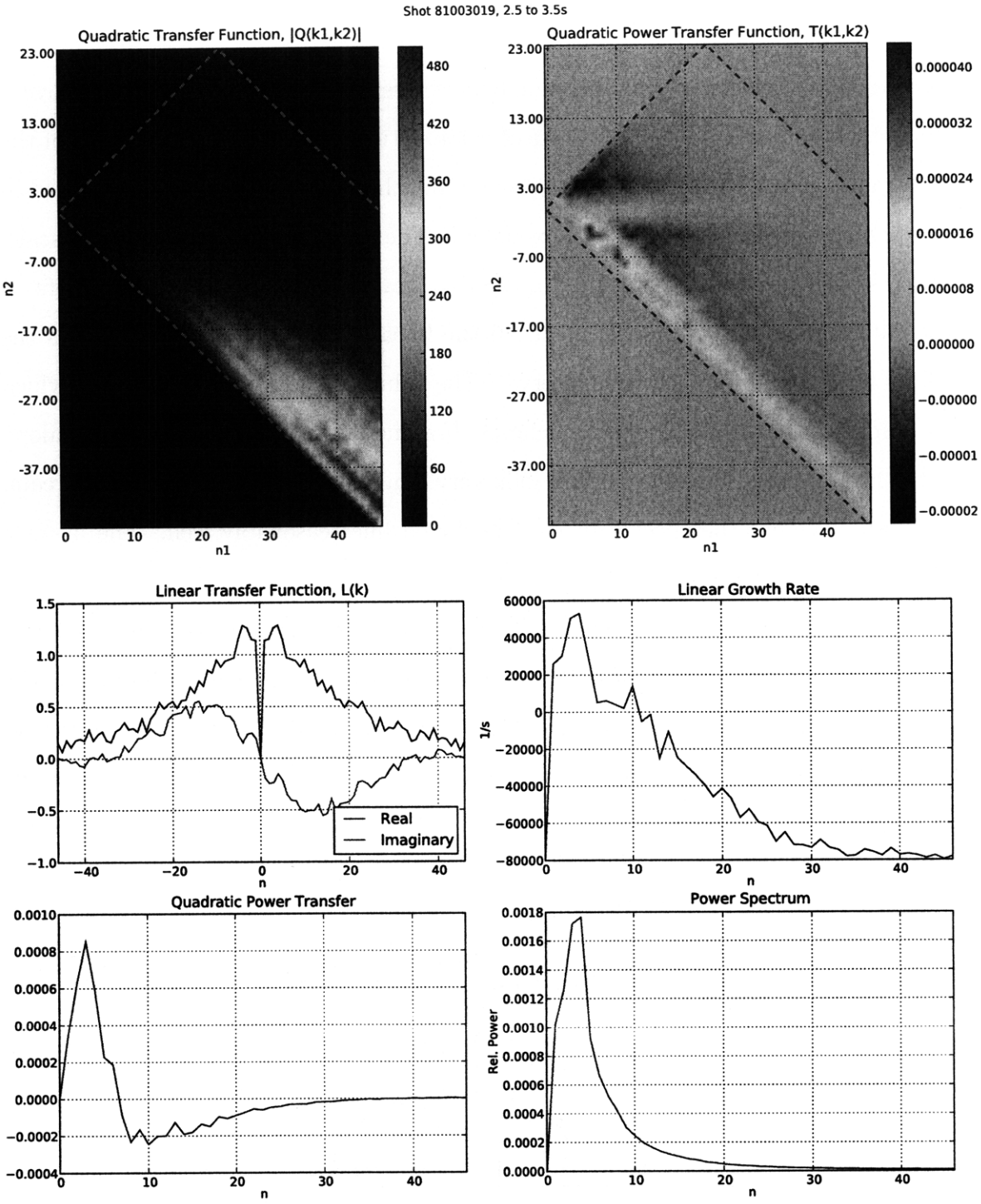

Figure 4-19: Results from applying the bispectral method in time instead of space. They match the spatial results from the previous subsection well.

4.4 Power Spectra

According to Kraichnan, the wavenumbers where energy is cascading away have a characteristic spectrum $\propto k^{-5/3}$. Fits of the function ax^b to the upper regions of the spectra are shown in the following figures. Only the shots and times that resulted in convergent bispectral analysis are examined. The data are plotted on log-log scale, which makes curves of the form ax^b appear as straight lines. The slope of lines fit to the data correspond to the exponent $b$in the linear case. Table 4.2 summarizes the values for b found for each time interval. The values range from -1.45 to -2.5, which encompasses the -1.66 value in Kraichnan. If a line of slope -1.66 were plotted along with the computed fits, they would look very similar, so it is not outside the realm of possibility that the spectra fit a -1.66 sloped line reasonably well. The average value of b from these six shots is -2.13.

There is a clear break in the spectrum's slope between high and low mode numbers in every plot. This implies that different processes are occurring in the low modes and high modes. In spectra from shots 9031202x and the 14.8-15.8 second interval of shot 81003019, the highest modes seem to have shallower slope and do not fall along the line fit to the middle modes.

Table 4.2: Summary of power fits.

Shot	Time	b
81003019	11.5 - 12.5	-1.45
	14.8 - 15.8	-2.545
81217011	0.5 - 1.5	-1.959
	15.5 - 16.5	-2.124
80312025	0.9 - 1.9	-2.35
80312028	1.0 - 2.0	-2.372

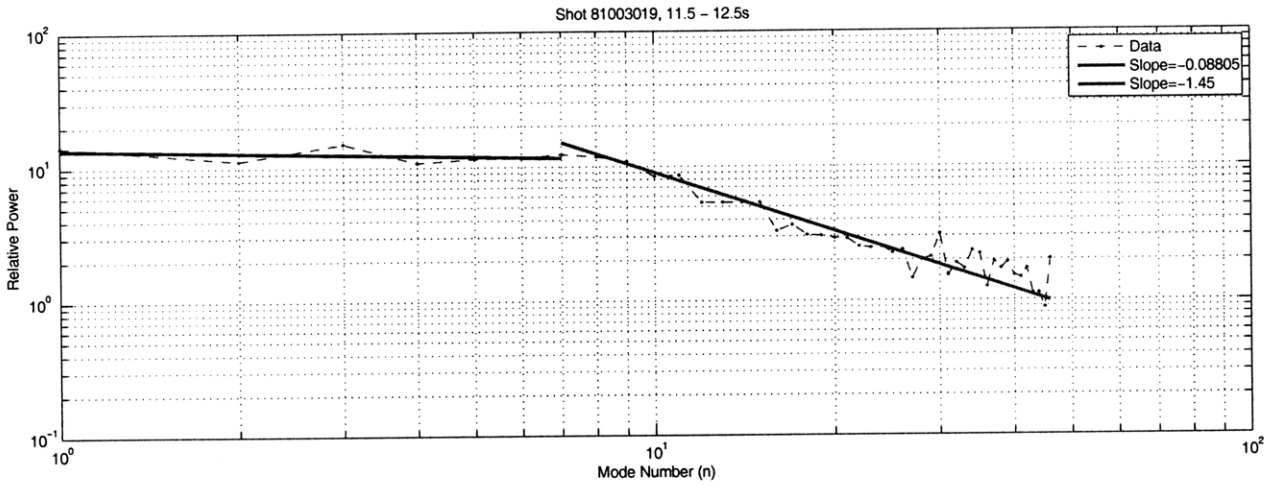

Figure 4-20: Power fit to large wavenumbers in shot 81003019.

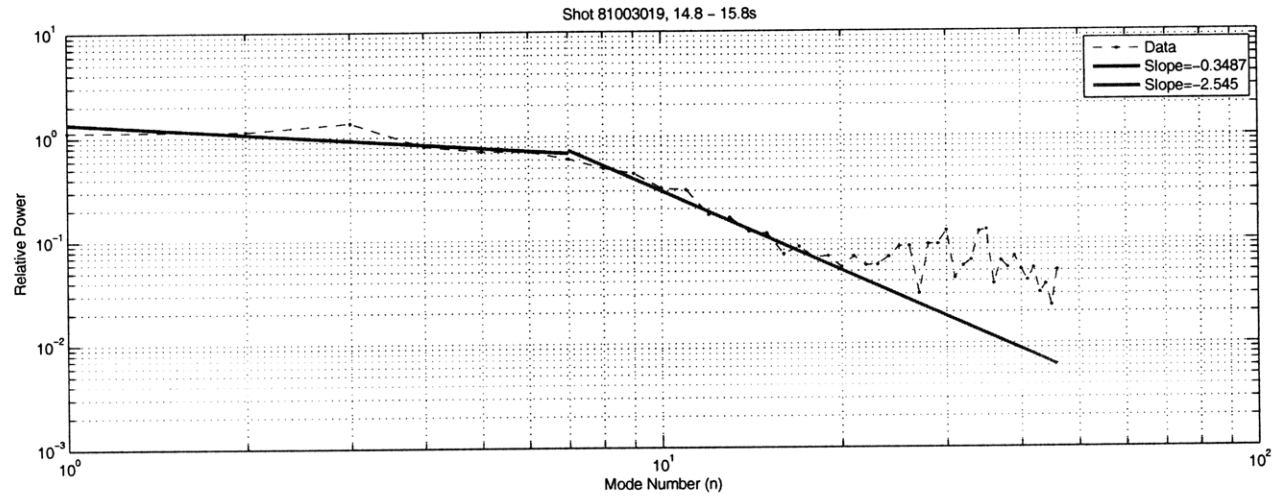

Figure 4-21: Power fit to large wavenumbers in shot 81003019.

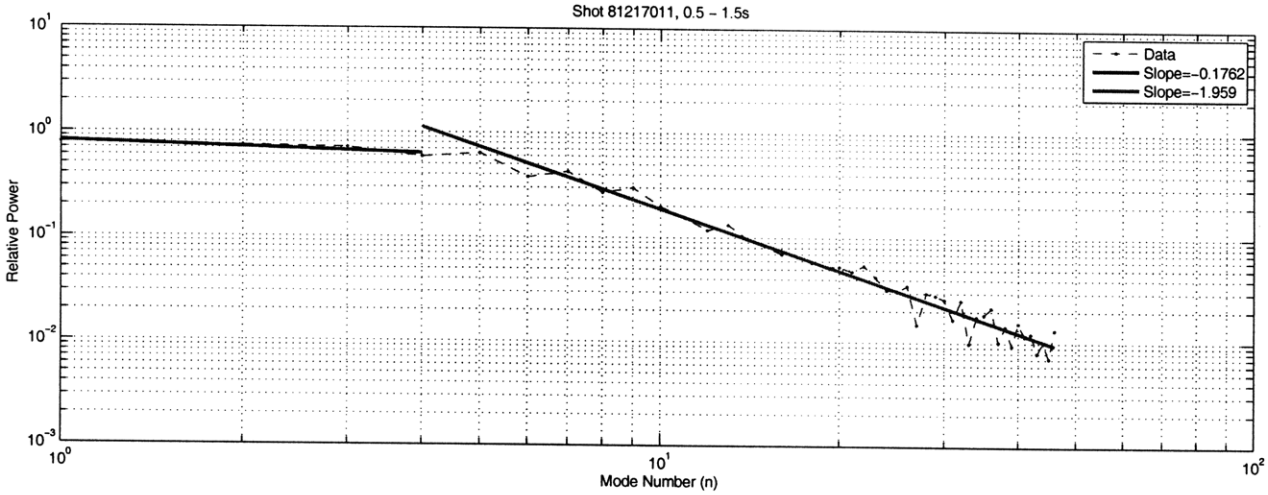

Figure 4-22: Power fit to large wavenumbers in shot 81217011.

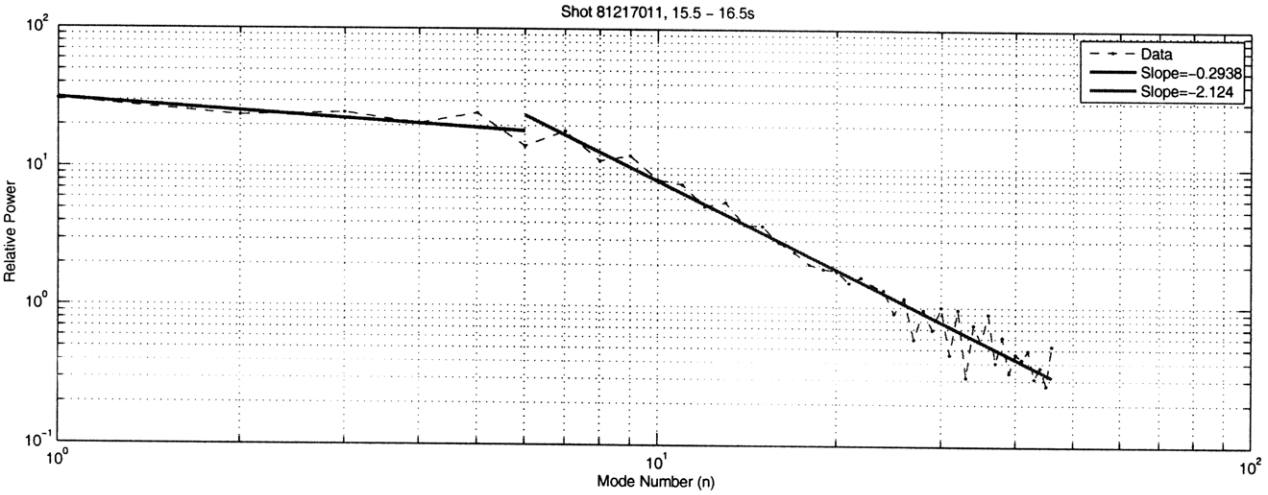

Figure 4-23: Power fit to large wavenumbers in shot 81217011.

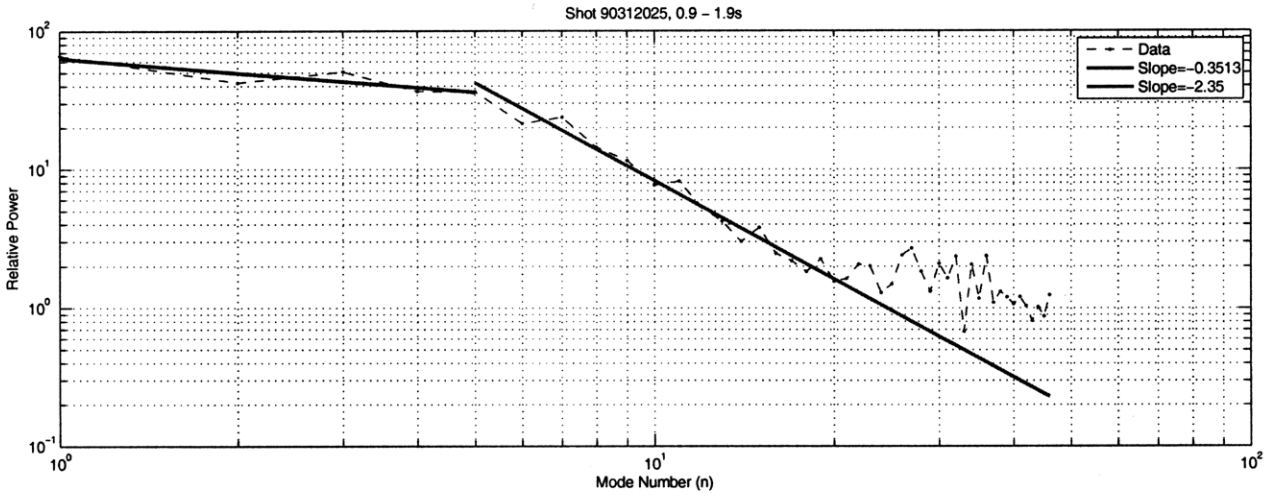

Figure 4-24: Power fit to large wavenumbers in shot 90312025.

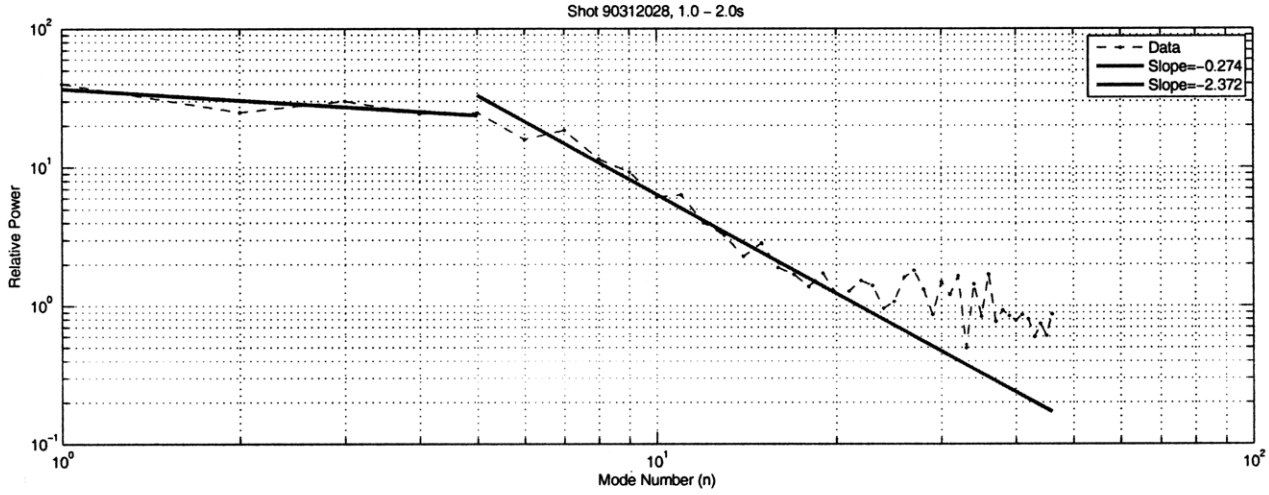

Figure 4-25: Power fit to large wavenumbers in shot 90312028.

Chapter 5

Conclusions

This is the first time that spatial modes have been directly measured in a dipole plasma, and overall the probe array functions very well as a diagnostic. It has very high signal-to-noise ratio, high frequency response, can measure wide range of potential, has modular/replaceable electronics, and has provided data suggestive of many predicted phenomena. The matching between the spatial and temporal bispectral analysis indicate that the two-point analysis done by Grierson, et. al. is valid for characterizing spatial modes in a dipolar plasma.

The spatial spectrograms show that odd, low mode numbers are dominant in LDX. These modes correspond directly to frequencies in time, as shown by both the temporal spectrograms and the linear dispersion relations in the bispectral analysis. The linear dispersion is consistent with a constant plasma rotational velocity, at least in the "toroidal" direction at a constant radius. The dispersion relation could be more complicated at different array elevations or at different radial positions. The average wavenumber power spectra span the $k^{-5/3}$ power law given by Kraichnan. This implies that the turbulence could be 2D in nature and that the inverse cascade of

energy shown by the bispectral plot is correct. The relation between time and space bispectral analysis and spectrograms suggest that the plasma is rotating, however. The instantaneous $E \times B$ radial drift velocities are the same magnitude as the ion sound speed, but average to near zero.

The bispectral analysis shows that the inverse energy cascade can occur in LDX plasmas. In the shot where it occurs, the linear growth rates show that wavenumbers on the order of 7-20 are excited by heating and their energy is transferred nonlinearly by way of three-wave coupling to lower wavenumbers on the order of 1-5. It can therefore be concluded that small-scale spatial structures transfer their energy to large-scale structures, which give rise to the large-scale potential fluctuations. The potential fluctuations cause radial $E \times B$ flows that average to near zero, meaning they form closed structures which are consistent with the notion of convective cells.

The quadratic coupling coefficient plots also show that small wavenumbers have very strong coupling to low wavenumbers. This may cause them to damp out immediately due to very strong nonlinear coupling, and therefore they are not present in the spectrum. Most of the power in the fluctuations, however, is not in very high wavenumbers, as shown by the power transfer plots, so they have minimal effect in the nonlinear power transfer. It could also be evidence that the inverse energy cascade is very much present in LDX since the power is concentrated in low modes. The higher modes are excited linearly and transferred to lower n values via nonlinear coupling of the waves.

The Ritz bispectral method does not always seem to work. This could be due to the disturbances RF heating impart on the plasma thus making the power spectrum continually varying, or that the plasma isn't normally stationary enough for the method to function correctly. The transfer functions were only convergent during 2.45GHz heating only or in the afterglow, never in times of strong heating. Another

reason could be that it is difficult for the method to differentiate quadratic and linear growth when there is very strong linear growth in low modes. Also, assuming that the off-diagonal terms in $\langle X^*_{k_1'} X^*_{k_2'} X_{k_1} X_{k_2} \rangle$ are zero might be a bad approximation in LDX.

The cascade is also only present when there is a high frequency component in the plasma. This can be seen directly from the spectrograms. This makes sense with the direction of the cascade, since there has to be power in the higher modes in order for it to be transferred away. Along the same lines, three wave coupling could explain why the strong low mode numbers are present in the two 090312x shots when the 10.5GHz source is turned on. If the source excites higher modes, its energy eventually ends up in a low mode.

Adding a radial arm to the array would enable a two-dimensional analysis to be conducted and both the toroidal and poloidal structure of the fluctuations determined. Then it could be found whether the toroidal fluctuations are constant in a flux tube or if they have some helicity to them. A whole new toroidal arm at another radius would also show if there is any velocity shear by showing if the dispersion changes slope at different radii. A 2D array would also provide a measure of vorticity, which could be compared to its predicted values to further validate the inverse cascade phenomena.

Another possible upgrade to the probe array would be to add ion saturation probes to measure the density fluctuations. This could be done by replacing every other probe, and reducing the resolution of both new arrays, or making new double-tipped probes that measure both ion saturation current and floating potential at every tip. This would be a more involved and expensive upgrade since the signal feedthrough and all probes would have to be replaced. Replacing every other probe would involve removing the series resistor in the array and making new amplifier

boards and backplanes to route the signals correctly.

An improvement to the analysis would be to use the method set forth by J. S. Kim, et al. in the paper "Technique for the experimental estimation of nonlinear energy transfer in fully developed turbulence." Their method modifies the Ritz method to reject non-ideal, non-quadratic interactions in the spectrum. It is therefore a more robust analysis that can measure the three-wave coupling in the presence of other phenomena, and would most likely yield better results from the probe array data [13]. Kim also starts with a matrix-based algorithm in the paper, and implementing this would speed up the analysis greatly. Currently, the analysis is run in Python using loops and takes about twelve hours to analyze run 1 second of array data. Using the Kim method and porting the routines to a compiled language would greatly increase the speed with which this analysis could be performed and produce more reliable results, thus allowing more data to be more accurately examined. The Kim method also computes the full fourth-order moment $\langle X^*_{k_1'} X^*_{k_2'} X_{k_1} X_{k_2} \rangle$, and therefore has one less assumption that can be violated.

Faster digitization would also improve the quality of the data analysis. One assumptions in the Ritz method is that the phase varies slowly in time and therefore the time differential of potential can be represented by a finite difference. Faster digitization would reduce the time between compared spectra and move the analysis further into the slowly varying phase regime. Another assumption is that the power spectrum is stationary. Faster digitization would ensure this by allowing the analysis to be done in smaller time frames, where things are more likely to be stationary. Going by the appearance of the stripey plots, the phase does not vary slowly. If it did, the stripey plots would look very smooth whereas they look very "digital" now and each "stripe" is only a few data points wide. If the digitization rate were made three to four times higher ($\approx$250-300KHz), the stripes would be substantially wider

and the slowly varying phase criteria would be more satisfactorily met.

Appendix A

Hardware

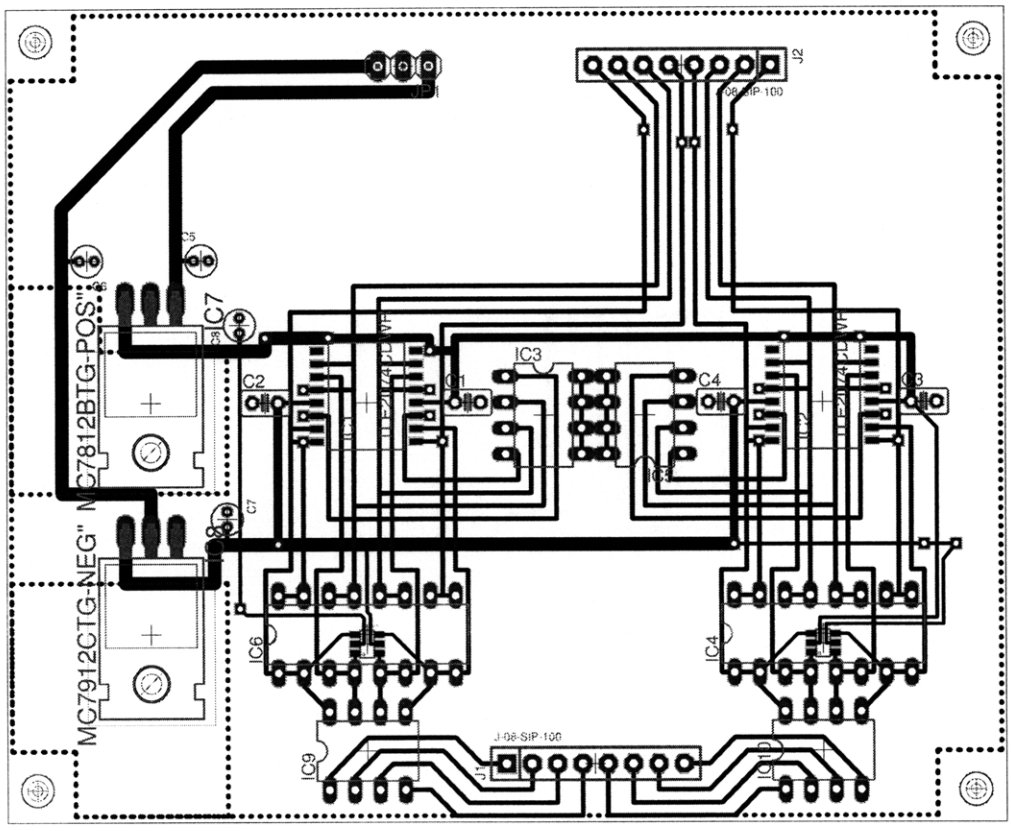

Figure A-1: Floating probe amp printed circut board layout

Bibliography

[1] Alexander C. Boxer. *Density Profiles of Plasmas Confined by the Field of a Levitating Dipole Magnet.* PhD dissertation, Massachusetts Institute of Technology, Department of Physics, 2008.

[2] D.T. Garnier et al. Stabilization of low frequency instability in a dipole plasma. *Journal of Plasma Physics*, 76(6):733–740, December 2008.

[3] Kesner et al. The dipole fusion confinement concept: A white paper for the fusion community. White paper, MIT, Plasma Science and Fusion Center, Cambridge, Massachusetts, 2007.

[4] Jeffrey Freidberg. *Plasma Physics and Fusion Energy.* Cambridge University Press, 2007.

[5] D.T. Garnier, A.C. Boxer, J.L. Ellsworth, J. Kesner, and M.E. Mauel. Confinement improvement with magnetic levitation of a superconducting dipole. *Nuclear Fusion*, 49(5):055023 (5pp), 2009.

[6] B. A. Grierson, M. W. Worstell, and M. E. Mauel. Global and local characterization of turbulent and chaotic structures in a dipole-confined plasma. *Physics of Plasmas*, 16(5):055902, 2009.

[7] David J. Griffiths. *Introduction to Electrodynamics.* Prentice Hall, 1999.

[8] A. Hasegawa and K. Mima. Pseudo-three-dimensional turbulence in magnetized nonuniform plasma. *Physics of Fluids*, 21:87–92, January 1978.

[9] Akira Hasegawa and Masahiro Wakatani. Plasma edge turbulence. *Phys. Rev. Lett.*, 50(9):682–686, Feb 1983.

[10] I.H. Hutchinson. *Principles of Plasma Diagnostics.* Cambridge University Press, 1987.

[11] M.J.R Schwar J.D. Swift. *Electrical Probe for Plasma Diagnostics.* American Elsevier, 1969.

[12] J. Kesner, D.T. Garnier, A. Hansen, M. Mauel, and L. Bromberg. Helium catalysed d-d fusion in a levitated dipole. *Nuclear Fusion*, 44(1):193–203, 2004.

[13] J. S. Kim, R. D. Durst, R. J. Fonck, E. Fernandez, A. Ware, and P. W. Terry. Technique for the experimental estimation of nonlinear energy transfer in fully developed turbulence. *Physics of Plasmas*, 3(11):3998–4009, 1996.

[14] S. Kobayashi, B. N. Rogers, and W. Dorland. Gyrokinetic simulations of turbulent transport in a ring dipole plasma. unsubmitted, March 2009.

[15] Robert H. Kraichnan. Inertial ranges in two-dimensional turbulence. *Physics of Fluids*, 10(7):1417–1423, 1967.

[16] Oliver Kreylos. Sampling theory 101, 2000. Web Resource.

[17] Dongsoo Lee, Yuk-Hong Ting, Lutfi Oksuz, and Noah Hershkowitz. Measurement of plasma potential fluctuations by emissive probes in cf4 radio-frequency plasma. *Plasma Sources Science and Technology*, 15(4):873–878, 2006.

[18] M. E. Mauel. Mhd interchange dynomics in straight field lines. Columbia University internal document, April 2008.

[19] V. P. Pastukhov and N. V. Chudin. Plasma convection near the threshold for mhd instability in nonparaxial magnetic confinement systems. *Plasma Physics Reports*, 27(11):907–921, 2001.

[20] Ch P Ritz and E J Powers. Estimation of nonlinear transfer functions for fully developed turbulence. *Phys. D*, 20(2-3):320–334, 1986.

[21] Ch. P. Ritz, E. J. Powers, and R. D. Bengtson. Experimental measurement of three-wave coupling and energy cascading. *Physics of Fluids B: Plasma Physics*, 1(1):153–163, 1989.

[22] J. Tonge, J. N. Leboeuf, C. Huang, and J. M. Dawson. Kinetic simulations of the stability of a plasma confined by the magnetic field of a current rod. *Physics of Plasmas*, 10(9):3475–3483, 2003.